Morphometry and mechanical instability at the onset of epithelial bladder cancer

Franziska L. Lampart[1,2], Roman Vetter[1,2], Kevin A. Yamauchi[1,2], Yifan Wang[1], Steve Runser[1,2], Nico Strohmeyer[1], Florian Meer[1], Marie-Didiée Hussherr[1], Gieri Camenisch[1], Hans-Helge Seifert[3], Cyrill A. Rentsch[3], Clémentine Le Magnen[3,4,5], Daniel J. Müller[1], Lukas Bubendorf[4], and Dagmar Iber[1,2,*]

[1]*Department of Biosystems Science and Engineering, ETH Zürich, Schanzenstrasse 44, 4056 Basel, Switzerland*
[2]*Swiss Institute of Bioinformatics, Schanzenstrasse 44, 4056 Basel, Switzerland*
[3]*Department of Urology, University Hospital Basel, Spitalstrasse 21, 4031 Basel, Switzerland*
[4]*Institute of Medical Genetics and Pathology, University Hospital Basel, Schönbeinstrasse 40, 4031 Basel, Switzerland*
[5]*Department of Biomedicine, University Hospital Basel, Hebelstrasse 20, 4031 Basel, Switzerland*
[*]*email: dagmar.iber@bsse.ethz.ch*

October 25, 2024

Malignancies of epithelial tissues, called carcinomas, account for most cancer cases. Research has largely focused on correlating different carcinoma subtypes to genetic alterations. However, besides a rewiring in the signaling networks, carcinoma progression is accompanied by mechanical changes in the epithelial cells and the extracellular matrix. Here, we reveal intricate morphologies in the basement membrane at the onset of bladder cancer and propose that they emerge from a mechanical instability upon epithelial overgrowth. We imaged mouse and human bladder tissue and performed differential growth simulations and found that stiffness changes in the different mucosa layers can result in aberrant tissue morphologies. The resulting thickening, wrinkles and folds resemble early papillary tumors and carcinomas *in situ*. Atomic force microscopy confirmed local stiffness changes in the pathological basement membrane. Our findings suggest a possible mechanical origin of the different bladder carcinoma subtypes and may guide future developments in treatment and prophylaxis.

Introduction

Carcinomas, the most common form of cancer [1], originate from epithelial tissues. Epithelia are thin tissues lining all body surfaces that rely on tight apical junctions for sealing and basal adhesion to the stiff basement membrane (BM) for stability [2, 3]. A hallmark of tumorigenesis is the local disintegration of the epithelial tissue architecture, which allows cells to breach the BM, a thin layer of extracellular matrix (ECM), and metastasise [4]. Deregulated epithelial growth can be inward (endophytic) or outward (exophytic), with the direction influencing tumor aggressiveness in organs like the bladder, kidney, skin and cervix [5–9]. While tumor growth patterns affect treatment decisions and post-treatment surveillance [10–13], the connection between genetic mutations and tumor morphology remains poorly understood [5], highlighting the need to explore physical drivers of tumor growth.

Bladder cancer (BC), among the most expensive cancers to manage [14], is ideal for studying epithelial morphogenesis at the onset of carcinogenesis due to its accessibility and ability to monitor tissue samples at various stages. The risk of urothelial BC invasion into deeper tissue layers depends on the growth pattern [15]. Papillary tumors form fingerlike protrusions either into the bladder lumen (exophytic growth) or, as inverted urothelial tumors, into the subepitheliale connective tissue (endophytic growth). Low-grade papillary tumors have a low risk of progression. In contrast, flat localised carcinoma *in situ* (CIS) (planophytic growth), have a high risk for progression to muscle-invasive BC [16, 17]. The N-Butyl-N-(4-hydroxybutyl) nitrosamine (BBN) mouse model allows for the observation of early BC progression, making it an ideal system to investigate the factors driving planophytic vs. exophytic growth.

Tissue curvature, as proposed recently for tubular epithelia in the pancreas of mice [6], can be ruled out as a reliable predictor for the growth of papillary vs. CIS in BC, as the bladder in mice and larger animals is too big, such that the tissue curvature is too low. Another important aspect is tissue mechanics. Tubular mucosa mechanically wrinkles under volumetric growth [18, 19]. The stiffness of the BM has been related to the emergence of either buds or folds in flat skin carcinomas [7]. Tumor-associated cells actively alter the structure and mechanical properties of the ECM [20–22]. Modifications to the tumor ECM impact cancer progression and treatment response [23, 24]. To become invasive and eventually metastasize, carcinomas must breach the BM. While proteases that remodel and degrade ECM components have been known to facilitate BM invasion [21, 25], recent research indicates that mechanical forces can also promote invasion independently of protease activity [26–28]. Despite the known changes in mechanical properties of the ECM [29–32] and ample evidence for the impact of ECM mechanics on cancer progression [21, 22, 29, 31, 33–35], the effect on the tumor morphology is not well understood.

Here, we combine continuum mechanics, 3D microscopy, and atomic force microscopy (AFM) to relate the BM morphologies that we uncover in the earliest BC stages to mechanical buckling, driven by urothelial overgrowth and changes in tissue stiffness. We characterize the morphological hallmarks of different BC subtypes in 3D imaging of human biopsies and mouse tissues and find that their onset can be recapitulated by continuum simulations of an elasto-plastic three-layered tissue undergoing differential growth. Changes in the composition and stiffness of the ECM in BC have already previously been investigated in the context of progression to muscle invasive BC and metastatic

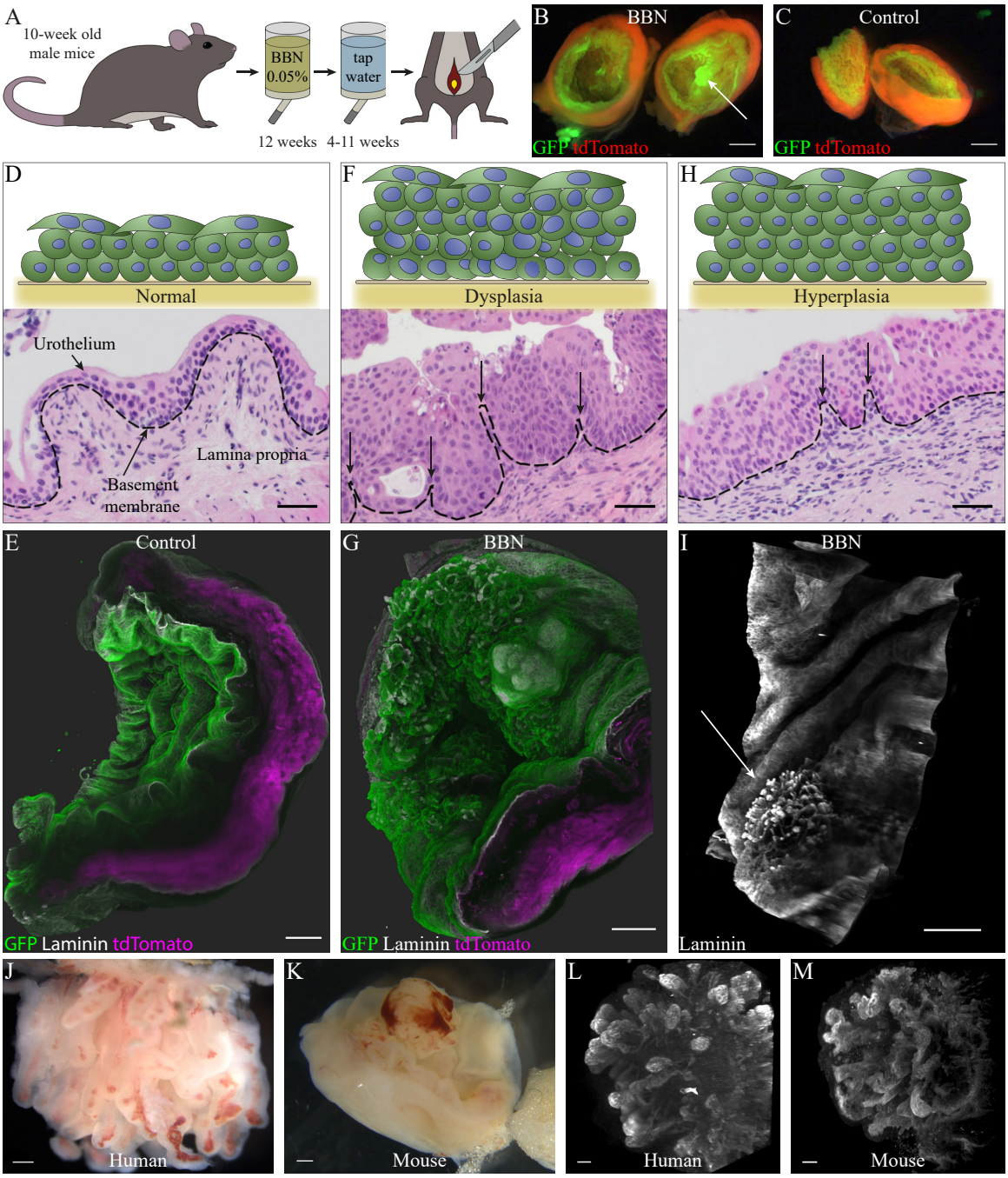

Figure 1: BBN induces changes in the mucosa of mice. (A) BBN treatment regime. (B–C) Macroscopic images of mouse bladders from treatment (B) and control (C) cohort, scale bar: 1 mm. (D) Illustration of a normal urothelium and histopathological section of mouse bladder tissue from the control cohort, scale bar: 50 µm. (E) 3D SPIM images showing the normal folding of a healthy mouse bladder mucosa, scale bar: 500 µm. (F) Illustration of a urothelium with dysplasia and histopathological section of mouse bladder tissue with dysplasia from the treatment cohort week 11 post BBN, scale bar: 50 µm. (G) 3D SPIM images showing the folding patterns of a mouse bladder mucosa from the treatment cohort at week 4 post BBN, scale bar: 500 µm. (H) Illustration of a urothelium with hyperplasia and histopathological section of mouse bladder tissue with hyperplasia from the treatment cohort week 4 post BBN, scale bar: 50 µm. Images show individual exemplary sections, not repeated experiments. (I) BM of a mouse tissue from the treated cohort at week 4 post BBN showing the localized fine grained buckling pattern in an area with neoplastic tissue growth, scale bar: 500 µm. (J–K) Biopsy of a human papillary tumor (J) and a BBN induced tumor in mice 11 weeks post BBN (K), scale bar: 500 µm. (L–M) BM structure in a human pTa tumor (L) and mouse bladder tumor (M), scale bar: 100 µm.

BC [36]. We now identify the relative stiffness of the three mucosa layers—the urothelium, the BM, and the lamina propria (LP)—as the main mechanical discriminant between exophytic and planophytic growth upon malignant proliferation of the epithelial cells. Consistent with this theory, AFM on mouse BMs confirms localised softening, which our model predicts to affect the growth pattern.

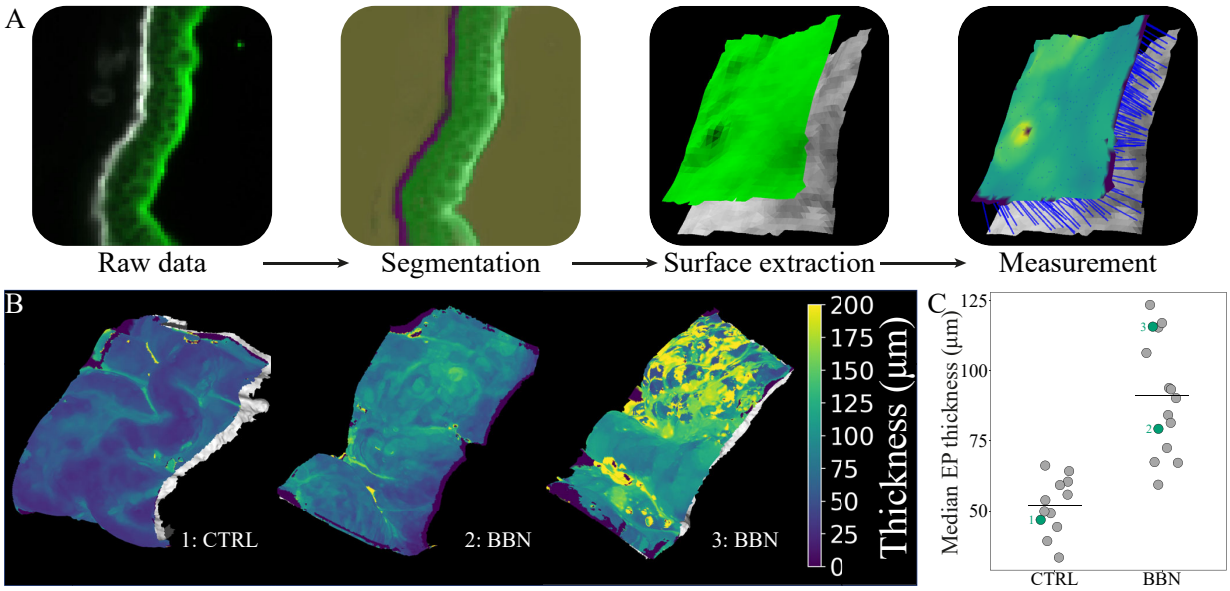

Figure 2: Thickness quantification of the urothelium. (A) Schematic representation of quantification pipeline used for thickness quantification. (B) Comparison of the urothelial thickness in control cohort mice and BBN treated mice 4 weeks post BBN. (C) Quantification of the thickness increase shows an almost two-fold increase in the thickness and a higher variance in the tissues from the BBN cohort. $n = 6$ control mice and $n = 8$ BBN mice 4 weeks after BBN stop (biological replicates). The green highlighted points correspond to the examples in (B).

Results

Early onset of bladder cancer visible in the structure of the basement membrane

To image the onset of BC, we chemically induced it by subjecting 10-week-old male mice that express a green fluorescent membrane marker (mEGFP) in the urothelial layer and a red fluorescent membrane marker (m-tdTomato) throughout the rest of the bladder tissue [37], to BBN in the drinking water (Fig. 1A,B, Methods). All bladders from the BBN treatment cohort showed alterations on the inside of the bladder wall 11 weeks after treatment. Macroscopically, they appear as nodular structures (Fig. 1B arrow). We encountered no such structures in bladders from the control cohort (Fig. 1C).

A healthy mouse urothelium is about three layers thick, and in the void bladder, the mucosa, consisting of the urothelium, the BM and LP, folds normally as seen in histopathological sections and the 3D reconstructions of single plane illumination microscopy (SPIM) z-stacks (Fig. 1D and E). 11 weeks after BBN treatment, various types of urothelial neoplasms emerge in the histopathological sections, such as dysplasia (Fig. 1F), a local overgrowth of cells with cytological atypia, papillary tumors and CIS (Extended Data Fig. 1A,B), with a thickening of the urothelium and abnormal-looking cells. In the dysplastic tissue, narrow folds of the BM and LP are visible (Fig. 1F, arrows), which are much smaller in diameter than the mucosa's typical bulging in a void bladder (Fig. 1D and E). These changes are also visible in 3D reconstructions of SPIM z-stacks from BBN cohort mice with neoplastic growth (Fig. 1G). Similar but smaller structures can be seen in bladders with hyperplasia, a local overgrowth of cells with normal cytological appearance, as early as 4 weeks after treatment (Fig. 1H, arrows). Here, the surrounding urothelium shows hyperplastic growth and thickening, but otherwise has normal cytological appearance (Fig. 1H), demonstrating that these narrow folds already arise in precancerous stages. The morphological changes become especially apparent in the BM, where a localized buckling pattern emerges that is noticeably different from the otherwise rather smooth BM (Fig. 1I, arrow).

In humans, papillary tumors grow into the eponymous shapes of long, finger-like protrusions with a fibrovascular core (Fig. 1J and Extended Data Fig. 1C,D). Mouse tumors do not form the elongated shapes seen in humans (Fig. 1K), possibly due to the spatial restrictions in the much smaller mouse bladder. Human bladder tumors have more space to grow into the bladder lumen, and even a non-invasive pTa tumor (Fig. 1J) can be of the size, or even larger than an entire mouse bladder. Nevertheless, in a biopsy from a noninvasive pTa tumor we found BM structures that have a striking similarity in size and shape to those in mice (Fig. 1L,M), suggesting that the structures described above represent the early onset of papillary BC.

Morphometric analysis of the urothelium

BC begins with urothelial thickening in the form of hyperplasia or dysplasia. Hyperplastic lesions are considered precursors of papillary tumors, while dysplastic lesions lead to CIS in BC [5]. We developed an image analysis pipeline to carry out morphometric analyses, in particular with regard to urothelial thickness and cell shapes (Fig. 2A, Methods). Control mouse bladder biopsies show a relatively uniform thickness profile and normal folding for an empty bladder (Fig. 2B, left). In contrast, mice 4 weeks after BBN treatment show various degrees of urothelial thickening, with the BM remaining either relatively smooth (Fig. 2B middle and Extended Data Fig. 2) or visibly roughing up (Fig. 2B right and Extended Data Fig. 2).

Consistent with previous findings, BBN-treated mice show a nearly twofold increase in mean urothelial thickness (91.2 ± 20.6 µm, SD) compared to controls (51.9 ± 10.0 µm, SD). Additionally, we observed greater variation in urothelial thickness both within and between bladders in BBN-treated mice compared to controls (Fig. 2C, Extended Data Fig. 2).

While hyperplasia and low-grade papillary tumors maintain relatively normal cellular appearance and tissue architecture, dysplasia, high-grade papillary tumors and CIS exhibit increasing cellular atypia and loss of polarity [38]. To quantify the extent of cellular atypia at early and late treatment stages, we

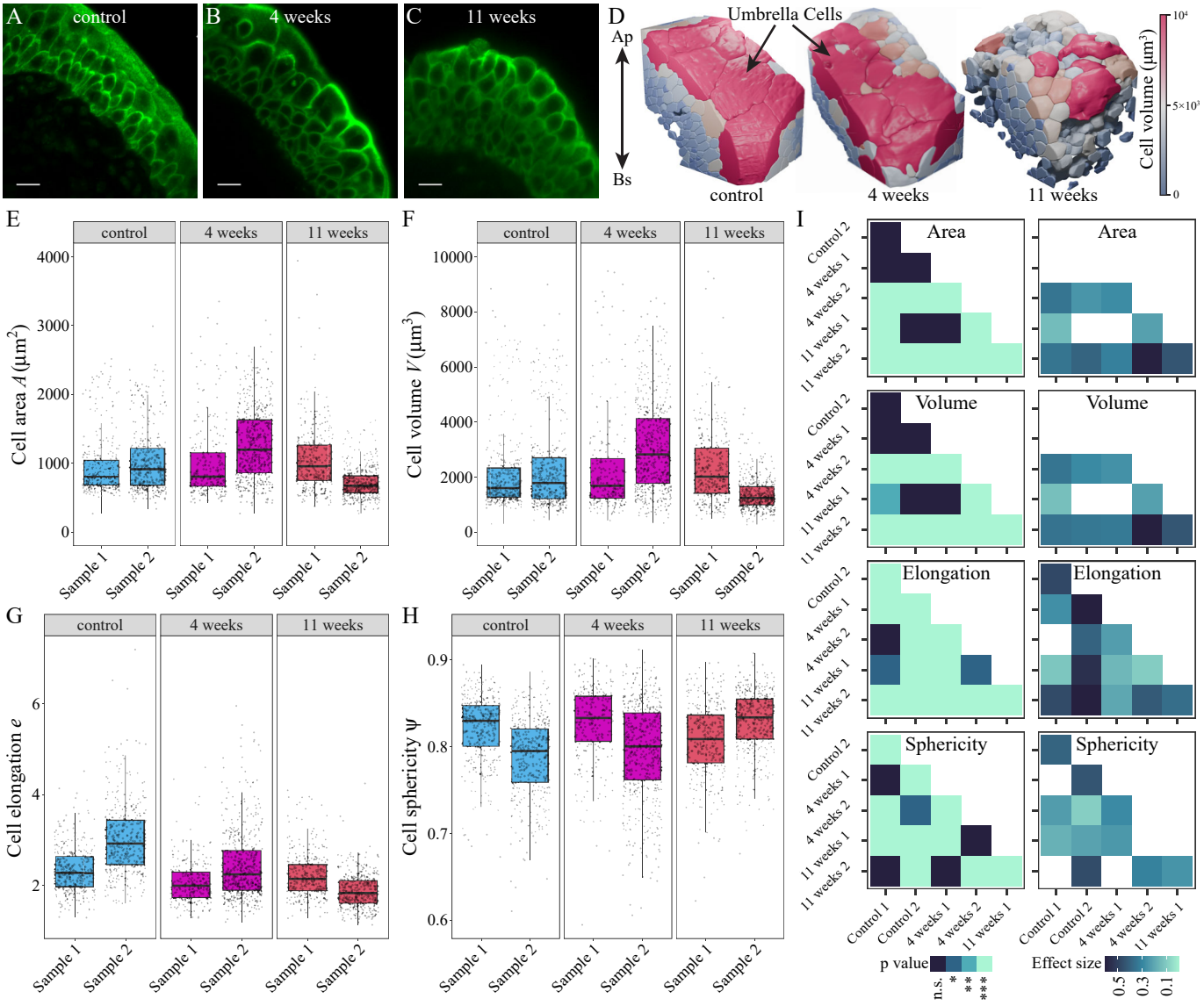

Figure 3: 3D morphometrics of urothelial cells. Two 3D SPIM images (samples) were analyzed for each condition. (A–C) 2D slices from sample 1 of the control cohort (A), from BBN treated mice 4 weeks post BBN (B) and from 11 weeks post BBN (C). Scale bar: 20 µm. Sample 2 images are shown in Extended Data Fig. 3. (D) 3D renderings of the segmented tissues displayed in (A–C). Ap; Apical, Bs; Basal. (E–H) Changes in cell membrane surface area A (E), cell volume V (F), elongation e (calculated as the ratio a/b from the major axis length a and the minor axis length b) (G) and sphericity $\Psi = \pi^{1/3}(6V)^{2/3}/A$ (H) of the 3D segmented urothelia. Box plots span first to third quartiles; middle line represents the median and whiskers show 1.5× the interquartile range. Number of cells (biological replicates): $n = 356$ (Control S1), $n = 388$ (Control S2), $n = 265$ (4-week BBN S1), $n = 529$ (4-week BBN S2), $n = 337$ (11-week BBN S1), $n = 417$ (11-week BBN S2). (I) Adjusted P values from Pairwise Wilcoxon test with Bonferroni correction for multiple testing and effect sizes corresponding to the box plots in (E–H). Significance levels: $P \leq 0.001$, ***; $P \leq 0.01$, **; $P \leq 0.05$, *; $P > 0.05$, n.s. Numerical values are listed in Supplementary Table 2.

3D-segmented cell boundaries in high-resolution images from two normal mouse bladders and two mouse bladders 4 and 11 weeks after BBN treatment, respectively. For each treatment endpoint, we analyzed one without (Fig. 3A–C) and one with buckling structures in detail (Extended Data Fig. 3A–C).

The samples from the BBN cohort display noticeable differences in the cell shape, such as enlarged (Fig. 3B) or elongated cells (Extended Data Fig. 3B), and a partial or complete loss of the umbrella cell layer (Fig. 3D), the outermost urothelial layer, as is typical for BC [38]. Some of these changes are also reflected in four analyzed morphological features (Fig. 3E–H, Supplementary Tables 1,2). However, these changes do not seem to be associated with samples that show papillary-like structures. Although both samples with visible protrusions display a significant change in area and volume with a medium to large effect size of > 0.3 (Fig. 3I), the changes are in opposite directions, with an increase in cell area and volume at 4 weeks and a decrease at 11 weeks (Fig. 3E–F, Sample 2). For the cell elongation and sphericity, the morphological analysis gives no coherent picture with significant differences and a large effect size even between the two control samples. Umbrella cells were excluded since they are generally missing in bladder tumors, and truncated due to their size in the segmentations in most cases. The lack of consistency suggests that changes in the tissue morphology are likely not a consequence of differences in cellular shapes at the onset of neoplastic growth.

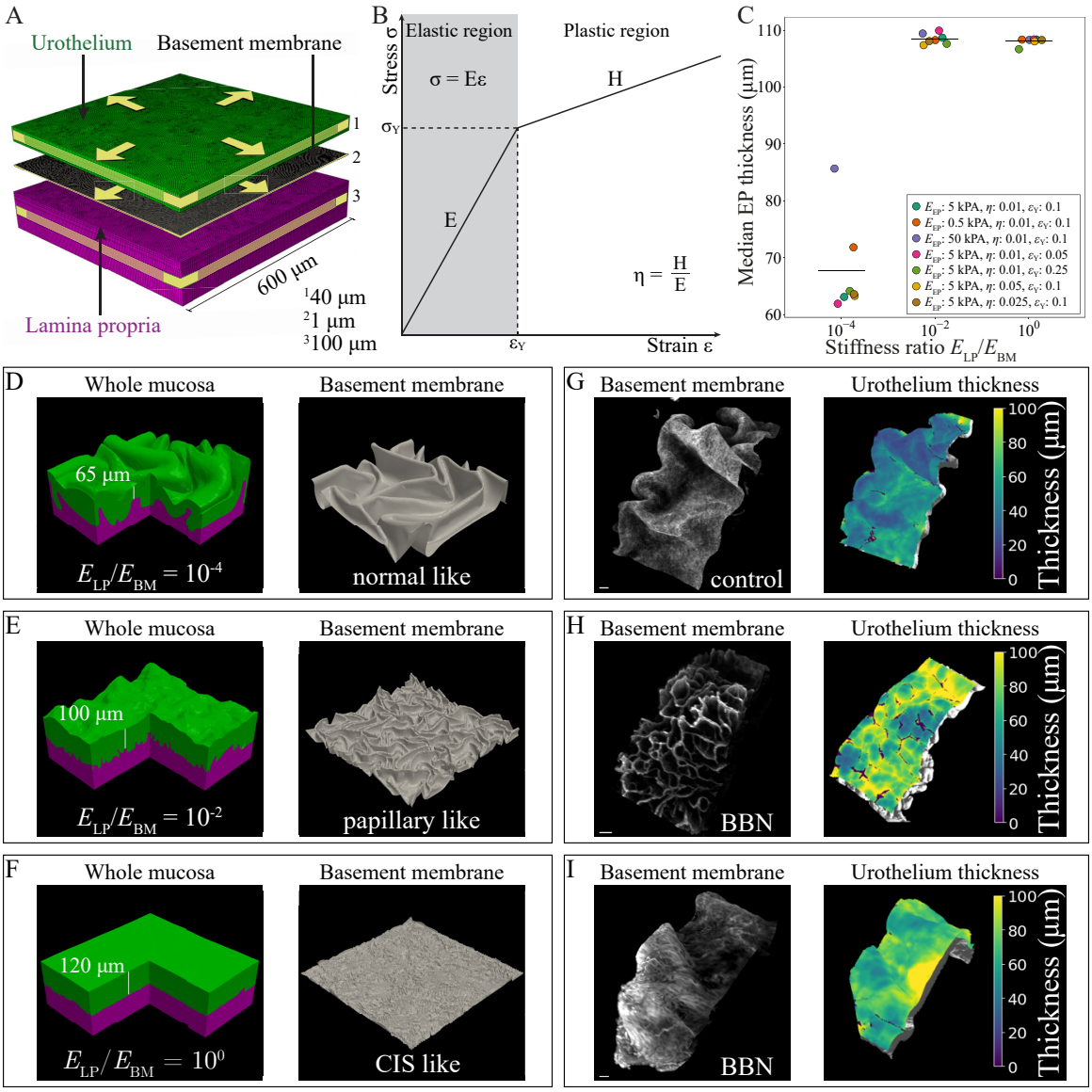

Figure 4: Different deformation modes in the BM depend on the stiffness of the LP and BM. (A) Schematic of the mechanical model setup, with volumetric expansion (yellow arrows) and boundary confinement (yellow bands). (B) Employed linear elasto-plastic constitutive stress-strain relationship. (C) Numerically observed thickening of the EP as a function of the stiffness ratio of the LP and BM. Detailed parameter description in Supplementary Table 3. $n = 7$ independent simulations per stiffness ratio. (D–F) Simulated mucosa morphologies at 50% expansion of the EP and BM in both in-plane directions, at indicated stiffness ratios, and corresponding BM shapes. $E_{EP} = 5$ kPa in (D–F), $E_{LP} = 5$ kPa in (D), $E_{LP} = 50$ kPa in (E), $E_{LP} = 500$ kPa in (F). Full parameter description in Supplementary Table 3. (G–I) Lightsheet microscopy images of the mouse bladder BM 4 weeks post BBN, showing normal smooth folding (G) and aberrant microscopic structures (H and I), and corresponding EP thickness profiles. Scale bar: 100 µm.

Mechanical simulations recapitulate different basement membrane morphologies

Thin elastic sheets and composites are known to exhibit a wealth of mechanical deformation modes under differential growth or compression [39–45]. Intestinal zig-zag patterns and villi, for instance, emerge from anisotropic growth and confinement of the multilayered mucosa [46, 47]. At large strains, secondary buckling modes can give rise to localized folding patterns [48–50] reminiscent of papillae. To explore whether the formation of the different BC morphologies could be of mechanical origin, we employed computational modeling (Methods). We simulated the continuum mechanics of planar 3D sections of the bladder mucosa, 600 × 600 µm in size, consisting of three tissue layers: a 40 µm thick epithelium (EP), a 1 µm thick BM and a 100 µm thick LP (Fig. 4A). Layer thicknesses vary between species; the human urothelium is about 45–110 µm thick [51]. A thickness of 40 µm for the EP layer was chosen as we start from a flat conformation in our simulations, corresponding to a non-empty mouse bladder. We simulated local volumetric tissue overgrowth by expanding the EP and BM layers slowly over time up to 50% in each of their two in-plane directions. Although somewhat compliant in reality, surrounding tissue will have a confining effect that we idealize as rigid here, irrespective of its state of health. Assuming incompressible, isotropic linear elasticity in all three layers for simplicity, the Young's moduli E_{EP}, E_{BM}, E_{LP} describe the stiffness of each layer. The assumption of an elastic BM is not only the simplest and thus parsimonious model, but also consistent with observations made in a long-term culture system, where the BM flattened to the degree that the

vasculature retracted (Supplementary Notes 1 and 2). Yet, to include structural rearrangements on the cellular or subcellular scale, made the EP and LP deform plastically beyond a plastic yield point $(\varepsilon_Y, \sigma_Y)$ (Fig. 4B, Methods).

In numerical simulations at different plastic hardening moduli and yield points, we found that a decreasing stiffness ratio E_{LP}/E_{BM} affects the extent of thickening of the urothelial layer (Fig. 4C), with a mean thickness of 67.7 ± 8.6 µm (SD) for $E_{LP}/E_{BM} = 10^{-4}$, 108.5 ± 0.9 µm (SD) for $E_{LP}/E_{BM} = 10^{-2}$ and 108.0 ± 0.6 µm (SD) for $E_{LP}/E_{BM} = 1$, and lets distinct folding patterns emerge in the BM (Fig. 4D, E and F). Changing the stiffness of the urothelium E_{EP} results in its thickening at $E_{LP}/E_{BM} \approx 10^{-4}$, while only marginally affecting the folding patterns (Extended Data Fig. 4). If E_{LP}/E_{BM} decreases (because the BM becomes stiffer or the LP softer), the BM pattern coarsens. At $E_{LP}/E_{BM} \approx 10^{-4}$, the morphology qualitatively resembles the normal smooth folding of the BM in an empty, healthy bladder (Fig. 4G). The undulations and folds transcend the BM and affect the entire urothelium, which thickens only little, similar to a normal urothelium in mice (Fig. 4G). At larger E_{LP}/E_{BM}, the folding occurs over shorter length scales, closer to the size of individual cells. At $E_{LP}/E_{BM} \approx 10^{-2}$, sharp folds with small amplitude dominate the pattern, but translate only into mesoscopic bumps on the apical surface of the urothelium (Fig. 4E). This BM morphology resembles that of BBN-treated mice, which can show networks of mesoscopic, papillary-like creases, and elevated EP thickness (Fig. 4H). At LP and BM stiffness parity, undulations on the apical surface of the EP disappear, and the majority of its volumetric expansion is translated into thickening. The BM exhibits microscopic folding and crumpling (Fig. 4F) akin to the fine-grained, non-uniform (CIS-like) structure observed atop the macroscopic folds in BBN-treated mice (Fig. 4I). The EP thickness profile in simulations agrees with the elevated but more uniform one observed in imaging (Fig. 4I).

Stiffness ratios govern mucosa folding modes

To obtain a more comprehensive, quantitative insight into the mucosa morphologies, and to further examine the potential of tissue mechanics to disrupt its structural integrity at the onset of BC formation, we sought a geometrical quantity that characterizes the emergent BM structure. We extracted the BM height maps (Fig. 5A) from SPIM images and simulations and Fourier-transformed them (Fig. 5B) to determine the geometrical spectrum of wrinkles and folds (Fig. 5C, Methods). The dominant wavelength λ_0 encodes the primary spatial separation between creases and furrows in the BM (Fig. 5A). The mechanical patterning is governed by relative stiffness ratios and layer thicknesses (Supplementary Note 3). Fixing all other model parameters, we computationally screened the space of mucosa deformations spanned by the stiffness ratios between the three layers, considering a substantially stiffer BM than the EP and LP [27]. This revealed a rich morphological phase space with two distinct regimes (Fig. 5D). At large values of E_{EP}/E_{BM} but small E_{LP}/E_{BM}, the comparably stiff expanding urothelium buckles and folds along with the BM, a regime we term "plate-like" EP deformation, characterized by undulations with large wavelengths in the order of ten cell diameters or more. Conversely, at comparably stiffer LP than EP, it is the BM alone that buckles and folds, with the EP and LP effectively acting as elastic media. In this "medium-like" EP deformation regime, disordered folds are observed in the BM with short wavelengths in the order of only a few cell diameters or even below a single cell diameter. An energy balance based on linear elasticity theory [52, 53] yields a morphological phase boundary between the two regimes (Fig. 5D,E, black dashed line; Supplementary Note 3). Traversing this boundary involves a continuous but steep change in λ_0 (Fig. 5D, colored contours). The critical wavelength along the transition line is proportional only to the epithelial thickness as a length scale, but declines with increasing tissue expansion (Supplementary Note 3). At fixed epithelial stiffness, the shape transition occurs along the E_{LP}/E_{BM} axis (Fig. 5E) with tighter folding toward larger E_{LP}/E_{BM}. Individual patterns and thickness quantifications are shown in Extended Data Figs. 5 and 6.

Plausible locations of the mouse and human bladder mucosa in the stiffness plane range from a vicinity of the morphological boundary toward greater E_{LP}/E_{EP} ratios. With tangent moduli of the urothelium in the order of 2–6 kPa [54] and about 2–3 orders of magnitude larger in the BM [55], the physiological region lies in the middle to upper right part of Fig. 5D.

Comparing numerical simulations with SPIM images of the mouse BM, we found a similar spectral footprint in the vertical displacement fields, although the numerical model rests on simplifying assumptions and does not reflect the biological inhomogeneity present in real tissues. In the power-law decay of the spectral amplitude $A \sim k^{-\alpha}$ and power spectral density $P \sim k^{-2\alpha}$ where k is the wavenumber (Methods), we observed a noise color that lies well beyond pink ($\alpha = 1$) and largely before red ($\alpha = 2$) in both the simulations and microscopy images (Fig. 5F). The pre-cancerous BM shape spectrum of BBN-treated mice quantitatively follows the same relationship between decay exponent α and dominant wavelength λ_0 as our simulations, whereas that of normal folds in control mice deviates substantially with greater α and λ_0 (Fig. 5F). Note that λ_0 is usually greater than the spacing between neighboring papillary protrusions and folds as seen in vertical tissue slices (Extended Data Fig. 7).

Simulations close to the morphological boundary yield troughs surrounded by ridges in the BM (Fig. 5G, top row) at $E_{EP}/E_{BM} \approx E_{LP}/E_{BM} \approx 10^{-3}$. For stiffer EP and LP (or softer BM), spot-like stress condensates are observed, with ridges connecting them at varying levels of BM elevation (Fig. 5G, bottom row)—a feature reminiscent of the onset of the finger-like protrusions in papillary tumor formation. Strikingly, these protrusions emerge facing the bladder lumen in the simulations like they do in papillary tumors (Extended Data Fig. 7). The folding pattern is sensitive to small stiffness changes, especially in the physiological region (Fig. 5D,H). For example, a $\approx$ 3-fold shortening of λ_0 can result from a $\approx$ 1.8-fold change in E_{LP}/E_{BM} and a $\approx$ 0.6-fold change in E_{EP}/E_{BM} (Fig. 5H, leftmost column).

Morphological transitions in the mucosa from a more normal folding to narrow crumpling can be induced by changing any of the three layer stiffnesses (Fig. 5H, right images), as only their ratios determine the pattern (Supplementary Note 3). Some possible pathways are a stiffening of the LP, a softening of the EP, or both of them concomitantly (Fig. 5D). But also a softening of the BM (and a stiffening of the LP) can lead to this transition (Fig 5E), suggesting that a combination of such changes can promote cancerous lesions. A softening of urothelial cells [56–58] and the upregulation of different ECM-related genes, linked to stiffening of the LP [36, 59, 60], have indeed been reported in BC and recognised as a risk factor for progression and invasion in BC.

Basement membrane softens locally in BBN-treated mice

As changes in the BM stiffness at the onset of bladder cancer had not been explored previously, we carried out AFM-based indentation measurement on decellularized mucosas from BBN-treated mice 4 weeks after treatment and from the control cohort (Fig. 6A). While the mean overall BM stiffness was only

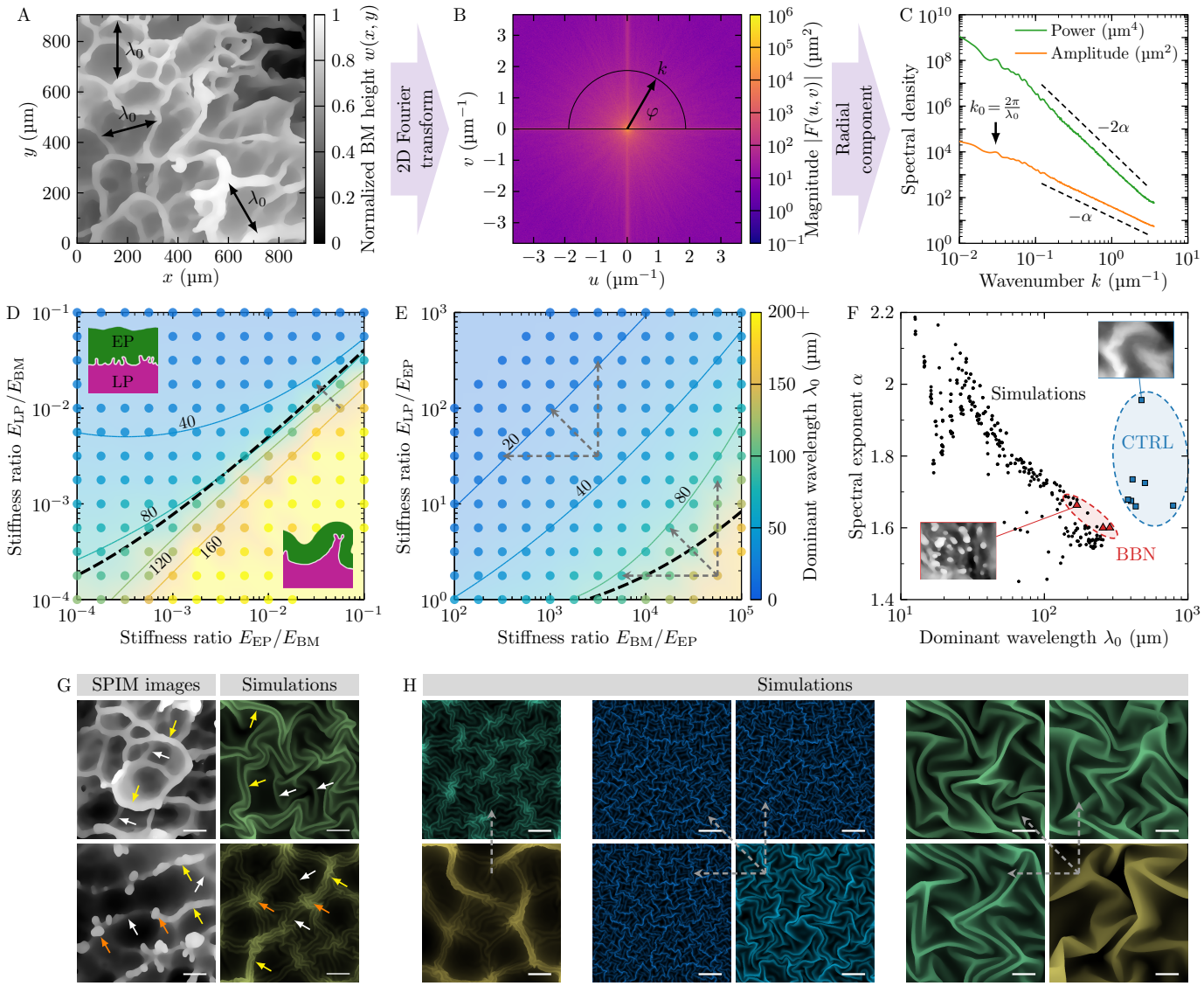

Figure 5: Morphogenetic analysis of BM buckling patterns. (A–C) Spectral analysis pipeline to extract morphogenetic characteristics of the BM structure. Vertical elevation maps of the (overhanging) triangulated BM meshes (A) are Fourier transformed (B). Averaging the magnitude (or its square) over all phase angles yields the isotropic spectral amplitude (or power spectral density), which decays algebraically with local peaks, the strongest of which defines the dominant wavelength λ_0 recognizable in the BM height map (A). Data from an exemplary BBN sample is shown in A–C. (D–E) Numerically obtained morphological phase diagram as a function of tissue stiffness ratios. Dots represent dominant wavelengths of individual simulations. Isolines are fitted parabolas at indicated wavelengths. Inset images show exemplary vertical slices of two deformation regimes, separated by a theoretical boundary (black dashed line, Supplementary Note 3). Simulation parameters: $h_{EP} = 40$ µm, $h_{BM} = 1$ µm, $h_{LP} = 100$ µm, $\eta_{EP} = 0.01$, $\eta_{LP} = 0.01$, $\epsilon_{Y,EP} = 0.1$, $\epsilon_{Y,LP} = 0.1$. Color scale in (E) applies to panels D and E. (F) Quantitative spectral comparison of BM morphologies between simulations (black dots) and SPIM images of control mice (blue squares) and BBN-treated mice (red triangles). Inset images show exemplary BM height maps for reference. (G) Two examples of vertical BM displacement out of three quantified SPIM images juxtaposed to simulations (top right: $E_{EP}/E_{BM} = 10^{-2.75}$, $E_{LP}/E_{BM} = 10^{-3}$; bottom right: $E_{EP}/E_{BM} = 10^{-1.5}$, $E_{LP}/E_{BM} = 10^{-2}$). Simulation images are colored by their λ_0. Qualitatively similar major and minor ridges (yellow and white arrows) surrounding dips of comparable size, and elevated spots (early papillary structures, orange arrows), some of which are linked by ridge folds, are marked. (H) Exemplary simulated BM height maps showing large structural differences over small stiffness changes. Dashed gray arrows show their location in panels D and E. Scale bars: 100 µm.

marginally softer in the BBN cohort (97±57 kPa, SD) compared to controls (120±44 kPa, SD), individual measurement positions in the BBN cohort displayed an almost 6-fold softening of the BM (20 ± 4 kPa, SD) compared to the overall stiffness in the controls (Fig. 6B, Supplementary Table 4). This suggests that BM softening does indeed occur locally already early during BBN treatment in mice.

Neither the measured local BM stiffness change nor the reported change in LP stiffness between normal tissue and matched BC tissues (3 kPa and 8 kPa, respectively [61]) are particularly pronounced when considered in isolation. Yet, in combination, E_{LP}/E_{BM} changes by more than an order of magnitude (16-fold), from ≈ 0.025 for the healthy condition to ≈ 0.4 for the cancerous conditions. In our simulations, a 10-fold change was enough to transition between the buckling modes, independent of whether these changes occur in the LP and/or the BM (Fig. 5E,H). Small changes in stiffness in different mucosa layers early during tumor development can have strong combined effects.

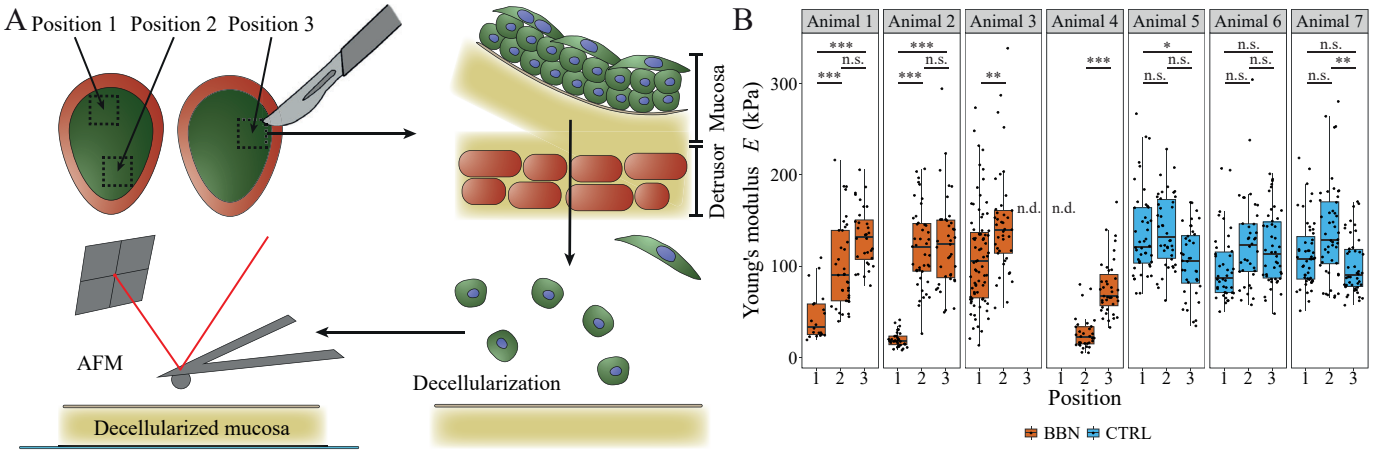

Figure 6: Atomic force microscopy reveals localized softening of the BM. (A) Visualization of the sample processing for AFM. (B) BM stiffness at 2–3 positions in bladders from the BBN treated cohort 4 weeks post BBN and corresponding control cohort mice, with adjusted P values from pairwise two-sided t-test with Bonferroni correction for multiple testing (numerical values in Supplementary Table 4). Significance levels: $P \leq 0.001$, ***; $P \leq 0.01$, **; $P \leq 0.05$, *; $P > 0.05$, n.s. Box plots span first to third quartiles, middle line represents the median and whiskers show 1.5× the interquartile range. Bladders from $n = 3$ control mice and $n = 4$ BBN mice (biological replicates) where probed at 2–3 positions each (Supplementary Table 4).

Discussion

We propose that a mechanical instability underlies the distinction between different bladder carcinoma subtypes. A morphological transition in the mucosa leads to distinct buckling patterns upon overgrowth of the urothelium. Intriguingly, the physiological regime lies near the morphological transition zone where structural changes require only small stiffness changes, hinting at a delicate constitutive balance between the mucosa layers. Perturbations of this balance accompanied by differential growth can disrupt the structural integrity of the bladder mucosa at the onset of BC formation, potentially shortening the patterning length scale down to the (sub)cellular level, where mechanical tissue damage may ensue. We found striking morphological agreement between the BM structure observed in simulations and in mice with developing BC, suggesting a mechanical basis for the emergence of papillary tumors and CIS. Our morphometric analysis revealed almost identical structures of the BM in the mouse and in humans, hinting at similar mechanical development during early papillary tumor growth.

Mechanical instabilities have previously been explored only in the context of tumor spheroids [62, 63]. Generally, solid mechanics models (for instance, coupling ECM mechanics to cellular behavior) remain underrepresented in cancer research [64, 65].

Our results echo with multilayered 2D vertex model simulations that found that stiffening of the BM promotes folding in skin cancer [7]. Our findings embed this result in a greater perspective of a mechanical patterning mechanism that explains not just single folds, but entire lesions. They also align with studies that have demonstrated that cells from more aggressive BC are softer [56–58]. The upregulation of type I and III collagen genes, predominantly found in the LP [66], is considered a marker for increased ECM stiffness and linked to BC invasion [36]. On the other hand, overexpression of the collagen IV proteases MMP2 and MMP9 have been recognized as a marker for BC progression [67]. Collagen IV is, besides Laminin, one of the main ECM proteins of the BM [66]. The degradation of collagen IV could explain why we observe localized BM softening in BBN mice. Our model predicts both a stiffening of the LP and a softening of the urothelium and BM to support lesion formation.

Our model is necessarily a simplification of the real mucosa and has limitations. For example, we do not take the vascularization of the LP into account, despite the known role of angiogenetic processes in many cancers, including BC [68]. We observed the vasculature to always follow the BM undulations in SPIM images. For the formation of elongated and branched structures, as seen in human papillary tumors, vascularization may thus also act as an additional driver or structural scaffold. Moreover, we assumed isotropic linear elasticity in all mucosa layers (with plastic strain hardening in the urothelium and LP to incorporate stress and strain localization due to the tissue's ability to relax stress with cellular rearrangements). While this is likely reasonably accurate for the near-threshold buckling behavior at the lesion onset, more elaborate constitutive behavior may be appropriate for large deformations of the bladder [69]. To enable a more quantitative morphometric comparison with tissue images, future mechanical modeling efforts could also benefit from a representation of heterogeneity in the growth pattern and mechanical properties in the mucosa, which we have not included here, but observed in AFM measurements (Fig. 6B). Experimental measurements of these are challenging, but would be a valuable acquisition in future research.

A recent study in rats [54] found that BBN treatment leads to a softening of the LP. This does not contradict our finding since, overall, the LP stiffens over the time course of the treatment as the rats age. The patient's age is one of the risk factors for BC development and progression [70], which could be reflected by the stiffening of the ECM due to ageing. Furthermore, urinary schistosomiasis [71] and previous radiotherapy of prostate cancer are known risk factors for developing BC [72, 73], both of which induce fibrosis in the bladder [71, 74]. Tissue stiffening due to transurethral resection (TURB) was proposed as a risk factor for BC progression [61]. This suggests that tumor-independent processes can also drive the stiffening of the LP in BC. While stiffness changes in the different mucosa layers were previously investigated mostly in the context of cancer progression, we demonstrate here that they could play an important role already at the onset. Further research is required to test this prediction experimentally, and to get a clearer picture of the magnitude, direction, timing, and causation of changes in the mechanical properties of the mucosa layers, and to what degree they are induced by the cancer itself or by cancer-independent processes.

For low-risk non-muscle-invasive BC, treatment usually con-

sists of TURB in combination with intravesical chemotherapy [17]. It has a good 5-year survival prognosis [75, 76]. However, BC often reoccurs and has a probability of 0.8%–45% to progress to muscle-invasive BC [15]. Especially CIS have a high risk for progression compared to papillary tumors [16, 17]. Although treatment options for muscle-invasive BC and metastatic disease have been expanded to immunotherapy and targeted therapies in recent years [77], the prognosis for survival remains substantially less favourable [76].

Incorporating stiffness measurements into the diagnostic process, e.g., through shear wave elasticity examinations [60] or AFM on biopsies [78], could help stratify patient risks and inform personalized treatment and monitoring regimes. In light of our study, the structural integrity and mechanical stability of the mucosa layers offers a promising line of attack for medical treatment and prophylaxis of BC progression.

Methods

Ethical Statement

Human BC biopsies were provided by the University Hospital of Basel (USB), Switzerland, under approval by the Ethical Committee of Northwestern and Central Switzerland (EKBB 37/13). Informed consent from all participants was obtained by the University Hospital of Basel.

All experiments involving animals were performed in accordance with the Swiss animal welfare legislation and approved by the veterinary office of the Canton Basel-Stadt, Switzerland (approval number 2957/29841). All animals were housed at the D-BSSE/University Basel facility under standard water, chow, enrichment, and 12-h light/dark cycles in a temperature (21±2°C) and humidity (55±10%) controlled room. An overview of all animals used in this study can be found in Supplementary Table 5.

Mouse strain and bladder cancer induction

To distinguish the urothelium from the other tissue layers in the bladder we used the $Shh^{Cre/+}$;$Rosa26^{mT/mG}$x RjOrl:SWISS crosses ($Shh^{Cre/+}$;$Rosa26^{mT/mG}$) previously described by Conrad et al. [37]. In these mice, the fluorescent marker m-tdTomato is expressed through the bladder tissue except in the urothelial layer, which expressed mEGFP.

BC can be induced in mice by spiking the drinking water with N-Butyl-N-(4-hydroxybutyl) nitrosamine (BBN) [79]. BBN is known to induce an inflammatory response already in the first weeks of treatment and BC few weeks after BBN stop [80]. The ideal sampling time point for early stages of BC was found to be 4 weeks post BBN. 11 weeks post BBN was defined as the latest sampling point to avoid suffering due to excessive tumor growth. In all our experimental setups, 10-week-old male mice were provided with 0.05% BBN (Sigma-Aldrich) in the drinking water for 12 weeks followed by 4–11 weeks normal drinking water. For the control condition, we used littermates maintained under identical housing conditions. To avoid suffering due to unwanted, excessive tumor growth mice were frequently monitored for signs of distress and body weight was controlled weekly. The maximum prospective degree of severity permitted was 2. None of the animals in this study exceeded the severity threshold and no animal had to be sacrificed due to exceeded tumor burden.

Mice were sacrificed at desired time point post BBN, and the bladders immediately harvested and washed in cold DPBS (Gibco). Excess fatty tissue was removed with surgical scissors and forceps before cutting the bladders sagittally into halves. For imaging, the bladder halves were fixed in 4% paraformaldehyde (PFA) (Thermo Fisher) for 3–4 h at 4°C and subsequently processed as described below. For tissues used in AFM, no PFA fixation was performed. Instead, bladder halves were submerged in Betadine solution (povidone-iodine 11 mg/mL, Mundi Pharma) for 1 min for disinfection and rinsed with DPBS. Further processing is described under the subsection AFM.

Optical clearing and immunofluorescence staining of fixed bladder tissue

Whole-mount tissue clearing of human and mouse biopsies was performed using the Clear Unobstructed Brain/Body Imaging Cocktails and Computational Analysis (CUBIC) protocol [81]. For better clearing and imaging, human and mouse biopsies were further cut into smaller sections if needed. Clearing times in reagents for decoloring, delipidation, permeation (CUBIC-1), and refractive index (RI) matching (CUBIC-2) were adjusted to maximize clearing efficiency and minimize quenching. Biopsies were incubated overnight in 50% CUBIC-1 (CUBIC-1:H_2O, v/v) at 37°C, followed by incubation in 100% CUBIC-1 for 5–10 days, depending on the biopsy's size, at 37°C on a nutating shaker. After optical clearing, the biopsies were washed three times in PBS on a rotating mixer for $>$ 1 h at room temperature (RT). All reagents used for preparation of CUBIC-1 and CUBIC-2 were obtained from Sigma-Aldrich, with the exception of N,N,N',N'-Tetrakis(2-hydroxypropyl)ethylenediamine (Tetrakis) obtained from TCI and Polyethylene glycol (PEG) mono-p-isooctylphenyl ether (Triton X-100) obtained from Nacalai Tesque (discontinued).

For immunofluorescent labelling, cleared biopsies were blocked for 3–4 h at room temperature (RT) or overnight at 4°C in blocking buffer (PBS (Sigma-Aldrich), 10% Fetal Bovine Serum (FBS) (Sigma-Aldrich), 1% Bovine Serum Albumin (BSA) (Sigma-Aldrich), 0.2% Triton X (Sigma-Aldrich) and 0.02% sodium azide (Sigma-Aldrich)). Blocked samples were then incubated with primary antibodies in blocking buffer for two nights at 4°C. After incubation with primary antibodies, samples were washed again with PBS three times for $>$ 1 h at RT on a rotating mixer and subsequently incubated again for two nights at 4°C with secondary antibodies in blocking buffer. For mouse tissues chicken anti-GFP polyclonal (Aves Labs; GFP-1020; 1:500) and rabbit anti-laminin polyclonal (Abcam; ab11575; 1:500) primary antibodies, and for human biopsies (Extended Data Fig. 1C and D) goat anti-ZO-1 polyclonal (Thermo Fisher; PA5-19090; 1:200) and anti-laminin polyclonal (Abcam; ab11575; 1:500) primary antibodies were used. As secondary antibodies the following fluorescently labelled antibodies were used: Alexa Fluor 488 goat anti-chicken IgG (Invitrogen; A11039; 1:500) and Alexa Fluor 647 donkey anti-rabbit IgG (Invitrogen; 32795; 1:500) for mice, and Alexa Fluor 488 donkey anti-goat IgG (Invitrogen; 11055; 1:500) and Alexa Fluor 647 donkey anti-rabbit IgG (Invitrogen; 32795; 1:500) for human biopsies.

At the end of the incubation, the samples were briefly washed in PBS before post-fixation for $>$ 15 min in 4% PFA at RT. To wash off the remaining PFA, the samples were washed three times for $>$ 15 min at RT in PBS before being placed in 50% CUBIC-2 (CUBIC-2:H_2O, v/v) overnight at RT, followed by 5–10 days in 100% CUBIC-2, depending on the biopsy's size.

Embedding and imaging cleared samples

Cleared samples were embedded in 2% low-melting-point solid agarose cylinders and first immersed in 50% CUBIC-2 for one night and then in 100% CUBIC-2 for up to two days. 3D image stacks were acquired using a Zeiss Lightsheet Z.1 SPIM and Zen 3.1 black software (Carl Zeiss Microscopy GmbH) using a 5x/0.16 clearing objective, and a clearing objective 20x/1.0 for the high-resolution images for cellular segmentation. For large

samples, tiled acquisition was used to image the whole sample. For each sample, laser powers and exposure times were adapted to the signal intensity to ensure optimal image quality for all acquisitions.

Image Processing and Analysis

Initial quality assessment of the images was done using Zen 3.1 blue (Carl Zeiss Microscopy GmbH). Tiled images were reconstructed using the Fiji [82] plugin BigStitcher [83]. For 3D visualization we used the software Imaris (Oxford Instruments).

For thickness quantification, single tiles were selected and scaled in Fiji, such that the xy pixel size matches the pixel size in z direction. To extract surface boundaries, we first performed pixel classification using the machine learning tool ilastik [84] to create tissue predictions for the urothelium and the BM. These predictions were put into a custom Python script to generate triangulated meshes. The meshed were subsequently post-processed and cleaned using MeshLab [85] and the integrated Screened Poisson Surface Reconstruction algorithm [86].

To approximate the thickness of the urothelium, we used a normal ray-based approach by projecting normal rays from the urothelium-lumen interface towards the urothelium-BM interface. The length of the rays to the point where they intersect with the urothelium-BM interface was then used to approximate the tissue-thickness of the given position (Fig. 2A). The surface meshes of the urothelium, with a color map representing the local thickness, and the BM were visualized using Napari [87]. The Python scripts are available as Jupyter notebooks (see Code Availability).

For the 3D segmentation, high-resolution images were first prefiltered using a custom Fiji macro and then segmented using PlantSeg 1.5.2 [88]. Curation and correction of the segmentations were done in Napari [87] using the morphometrics plugin [89]. Morphometric analysis and meshing were performed with customized Python scripts, and the mesh visualization was created in Blender 4.0 [90]. The Fiji macro and Python scripts are available from our public repository (see Code Availability).

Numerical Simulations

We simulated the nonlinear mechanical deformation of the mucosa in response to differential volumetric growth using the finite element method in Abaqus FEA 2021 (Dassault Systèmes). Model files are provided (see Code Availability). The mucosa was represented as a three-layered continuum consisting of the EP, the BM and the LP, from top to bottom, tied together with continuous displacement fields. We simulated square tissue sections with an edge length of 600 µm, and initial layer thicknesses $h_{\mathrm{EP}} = 40$ µm, $h_{\mathrm{BM}} = 1$ µm and $h_{\mathrm{LP}} = 100$ µm (Fig. 4A). At the four lateral sides of the simulated square mucosa patch, we fixed the displacement of all three layers in normal direction to mimic confinement by the surrounding tissue. In addition, the vertical displacement of the bottom surface of the LP was also constrained to zero, as the mucosa is connected to subjacent muscular tissue there. To mimic epithelial proliferation, we expanded the volumes of the EP and BM layers orthotropically by 50% in each of their planar directions, but not vertically, resulting in a total volumetric fold-change of 2.25 in these two layers. In response to the stresses caused by this differential growth and the confined tissue boundaries, the mucosa buckled out of plane. Note that our simulations are limited to the case with epithelial overgrowth and do not capture the control bladders. Simulating the folding of healthy empty bladders would likely require a different model setup.

In absence of detailed knowledge on the exact constitutive relationships in healthy and cancerous mucosa, we sought to build a minimal model that is sufficient to capture the essence of the mechanical phenomena at the onset of bladder cancer formation. We therefore assumed isotropic, homogeneous, linearly elasto-plastic behavior in all three layers. For a more detailed discussion of constitutive bladder models, see [69]. The stiffness in the elastic deformation of each layer (modeled with Hooke's law in 3D) was set by their Young's moduli E_{EP}, E_{BM} and E_{LP}. To make the mucosa nearly incompressible, we fixed all Poisson ratios at $\nu = 0.48$. To enable large deformations far beyond the buckling threshold, local stress relaxation at the cellular or sub-cellular level was incorporated in our model by making the EP and LP plastic upon reaching a von Mises stress yield stress [91] $\sigma_{\mathrm{Y}} = E\epsilon_{\mathrm{Y}}$, where ϵ_{Y} is an effective yield strain (Fig. 4B). We fixed $\epsilon_{\mathrm{Y}} = 0.1$ in both the EP and LP, a value that can be quickly reached as the EP and BM expand by 50% in both of their planar directions. In the plastic regime, linear strain hardening [91] was assumed for simplicity, with isotropic hardening moduli H_{EP} and H_{LP}. We kept the ratios $H_{\mathrm{EP}}/E_{\mathrm{EP}} = H_{\mathrm{LP}}/E_{\mathrm{LP}} = 0.01$ fixed in all simulations, except where specified otherwise.

The EP and LP were modeled as solids, discretized into 125,111 and 142,984 hexahedra (element type C3D8R), respectively. The BM was modeled as a thin shell consisting of 78,239 triangles (element type S3R). We explicitly solved Newton's damped second law, making sure that inertial and viscous forces remained small throughout (quasi-static regime).

Spectral analysis of the wrinkling pattern

Upon complete volumetric expansion, we extracted normalized vertical displacement maps $w(x, y) \in [0, 1]$ of the BM in parallel projections as seen from the top (Fig. 5A), at a resolution of 1.2 pixel/µm. As our simulations were geometrically fully nonlinear, the simulated BMs can overhang (Fig. 5D and Extended Data Fig. 7), just like in the lightsheet images. To quantify the tissue morphologies, we performed a spectral analysis on the height maps using the 2D Fourier transform (Fig. 5B),

$$F(u, v) = \int_{-\infty}^{\infty} \int_{-\infty}^{\infty} w(x, y) e^{-i(ux+vy)}\, dx\, dy.$$

$F(u, v)$ is generally complex, and the spectral magnitude $|F(u, v)|$ encodes periodic undulations in the BM with wave vector $\vec{k} = (u, v)$. To extract the isotropic (radial) component in the wrinkling pattern, we averaged the amplitude and power spectra over all polar angles:

$$A(k) = \frac{1}{\pi} \int_0^{\pi} |F(k\cos\varphi, k\sin\varphi)|\, d\varphi,$$
$$S(k) = \frac{1}{\pi} \int_0^{\pi} |F(k\cos\varphi, k\sin\varphi)|^2\, d\varphi,$$

where $k = \sqrt{u^2 + v^2}$ is the wavenumber. By virtue of the Wiener–Khinchin theorem, these spectra can be interpreted as measures of isotropic spatial autocorrelation in the vertical displacement field of the BM. Globally, they decay algebraically for increasing wavenumbers ($A \sim k^{-\alpha}$, $S \sim k^{-2\alpha}$), exhibiting local peaks at discrete wavelengths $\lambda_i = 2\pi/k_i$, $i = 0, 1, ...$ (Fig. 5C). The wavelength with largest amplitude, λ_0, quantifies the primary buckling mode, and served as a scalar measure of the main average spatial separation between wrinkles or folds in the mucosa (Fig. 5D and E). In practice, identifying k_0 can be ambiguous, as several nearby peaks away from the power law can have similar amplitude. To extract it robustly, we followed a heuristic approach by fitting Gaussian curves $a\exp[-(\ln k/k_0)^2/2\sigma^2] + c$ to $A(k)k$ with the DC component removed, where k_0,a,σ,c are free parameters. The same procedure was applied to the SPIM

images of three BBN samples with visible lesions and seven control samples with normal mucosa folding (Fig. 5F). The spectral analysis was performed in Matlab R2023b (The MathWorks).

AFM-based indentation measurement

Bladder halves were further cut into approximately 3×3 mm specimens. Using fine forceps, the mucosa was carefully peeled off the detrusor. From each of the three control bladders, we selected three mucosa specimens from different locations of the bladder. Since the mucosa seems to be more fragile in BBN-treated mice, we were only able to obtain 2 mucosa specimens from two of the four mice from the BBN-treatment cohort. From the remaining two bladders, three mucosa specimens were obtained. For decellularization, the mucosas were submerged in a sterile 0.1% sodium dodecyl sulfate (SDS) (Sigma-Aldrich) solution and incubated at RT for 72 h on a rotating mixer. We used an SDS-based approach as it preserves the physiological properties well enough that the matrix can still be used for *in vitro* tissue-engineering and *in vivo* bladder grafts [92, 93]. The SDS solution was refreshed every 24 h. After that, the mucosas were washed in sterile water for 72 h at RT on a rotating mixer and the water was replaced every 24 h. The decellularized mucosas were placed on a 35 mm glass bottom petri dish (World Precission Instruments) with the BM facing upwards. To improve adhesion, excess water was left to evaporate 5 min, so that the mucosas stick to the petri dish, before the dish was filled with sterile water.

An AFM (NanoWizzardII, JPK, Germany) was mounted onto an inverted light microscope (Observer Z1, Zeiss, Germany). A tipless triangular cantilever (NPO-D, Bruker, US) with a 5 µm diameter bead attached to its apex was used for the measurements. The spring constant of the cantilever was determined by the thermal noise method. For indentation experiments, the beaded cantilever was positioned above an area of interest. A grid of 4×4 positions within 100×100 µm was defined for indentation experiments. The beaded cantilever was approached to the sample at 5 µm/s until a force of 10 nN was recorded. Subsequently, the cantilever was retracted and moved to the next position in the grid. Three different regions per sample were tested if possible. Data analysis was performed with the inbuilt JPK Data Analysis software. The recorded force-distance curves of the approach were offset and tilt corrected and corrected for the cantilever deflection. Afterwards, the approach force-distance curve was fitted by the Hertz model with a Poisson ratio of $\nu = 0.5$. The contact point in FD curves was determined automatically.

Acknowledgements

This work was funded by PHRT iDoc grant 306 to D.I., C.A.R. and L.B. and SNF Sinergia grant CRSII5_170930 to D.I. The authors thank Radhe Kumar and Antanas Murelis for their contributions as part of their student projects, the imaging facility of the D-BSSE for training and technical support, and the members of the Iber group for valuable discussions.

Author Contributions

D.I., F.L.L., R.V., C.L.M, L.B., C.A.R., H-H.S., and D.J.M. designed the research; F.L.L., M-D.H. and G.C. performed animal experiments; C.A.R. provided human tumor biopsies; L.B. performed tumor staging and grading on human and mouse tumors; F.L.L. generated all imaging data; F.L.L., K.A.Y and S.R. analyzed the imaging data; R.V., F.L.L., Y.W., F.M. and D.I. developed, simulated, and analysed the computational model; N.S. and F.L.L. carried out the AFM measurements; F.L.L., R.V., K.A.Y, N.S. and D.I wrote the manuscript; F.L.L., R.V., Y.W. S.R. created the figures.

Competing Interests

The authors declare no competing interests.

Data Availability

Raw images are available as a publicly accessible openBIS repository at `https://u.ethz.ch/cxOpQ`.

Code Availability

The source code is publicly released under the 3-clause BSD license as a git repository at `https://git.bsse.ethz.ch/iber/Publications/2023_lampart_bladder_cancer`.

References

[1] H. Sung, J. Ferlay, R. L. Siegel, M. Laversanne, I. Soerjomataram, et al. Global Cancer Statistics 2020: GLOBOCAN Estimates of Incidence and Mortality Worldwide for 36 Cancers in 185 Countries. *CA Cancer J. Clin.*, 71: 209–249, 2021. doi: 10.3322/caac.21660.

[2] E. Knust and O. Bossinger. Composition and Formation of Intercellular Junctions in Epithelial Cells. *Science*, 298: 1955–1959, 2002. doi: 10.1126/science.1072161.

[3] M. A. Morrissey and D. R. Sherwood. An active role for basement membrane assembly and modification in tissue sculpting. *J.Cell Sci.*, 128:1661–1668, 2015. doi: 10.1242/jcs.168021.

[4] Y. A. Fouad and C. Aanei. Revisiting the hallmarks of cancer. *Am. J. Cancer Res.*, 7:1016–1036, 2017.

[5] O. Sanli, J. Dobruch, M. A. Knowles, M. Burger, M. Alemozaffar, et al. Bladder cancer. *Nat. Rev. Dis. Primers*, 3: 1–19, 2017. doi: 10.1038/nrdp.2017.22.

[6] H. A. Messal, S. Alt, R. M. M. Ferreira, C. Gribben, V. M.-Y. Wang, et al. Tissue curvature and apicobasal mechanical tension imbalance instruct cancer morphogenesis. *Nature*, 566:126–130, 2019. doi: 10.1038/s41586-019-0891-2.

[7] V. F. Fiore, M. Krajnc, F. Garcia Quiroz, J. Levorse, H. A. Pasolli, et al. Mechanics of a multilayer epithelium instruct tumour architecture and function. *Nature*, 585:433–439, 2020. doi: 10.1038/s41586-020-2695-9.

[8] J. D. Trelford, A. D. Tsodikov, and A. Y. Yakovlev. Modeling post-treatment development of cervical carcinoma: exophytic or endophytic — does it matter? *Math. Comput. Model.*, 33:1439–1443, 2001. doi: 10.1016/S0895-7177(01)80025-X.

[9] M. Kim, S. Ishioka, T. Endo, T. Baba, M. Mizuuchi, et al. Possibility of less radical treatment for patients with early invasive uterine cervical cancer. *J. Obstet. Gynaecol.*, 42: 876–882, 2016. doi: 10.1111/jog.12980.

[10] A. Kutikov and R. G. Uzzo. The R.E.N.A.L. Nephrometry Score: A Comprehensive Standardized System for Quantitating Renal Tumor Size, Location and Depth. *J. Urol.*, 182:844–853, 2009. doi: 10.1016/j.juro.2009.05.035.

[11] R. Rao and S. G. Honavar. Retinoblastoma. *Indian J. Pediatr.*, 84:937–944, 2017. doi: 10.1007/s12098-017-2395-0.

[12] L. M. Smid, K. A. van Overdam, V. Davidoiu, J. H. de Jong, J. F. de Boer, et al. Classification and treatment follow-up of a juxtapapillary retinal hemangioblastoma with optical coherence tomography angiography. *Am. J. Ophthalmol. Case Rep.*, 15:100472, 2019. doi: 10.1016/j.ajoc.2019.100472.

[13] V. A. Capozzi, E. Scarpelli, L. Monfardini, V. D. Mandato, C. Merisio, et al. Do Exophytic and Endophytic Patterns in Borderline Ovarian Tumors Have Different Prognostic Implications? A Large Multicentric Experience. *J. Clin. Med.*, 12:3544, 2023. doi: 10.3390/jcm12103544.

[14] R. S. Svatek, B. K. Hollenbeck, S. Holmäng, R. Lee, S. P. Kim, et al. The Economics of Bladder Cancer: Costs and Considerations of Caring for This Disease. *Eur. Urol.*, 66: 253–262, 2014. doi: 10.1016/j.eururo.2014.01.006.

[15] R. J. Sylvester, A. P. M. van der Meijden, W. Oosterlinck, J. A. Witjes, C. Bouffioux, et al. Predicting Recurrence and Progression in Individual Patients with Stage Ta T1 Bladder Cancer Using EORTC Risk Tables: A Combined Analysis of 2596 Patients from Seven EORTC Trials. *Eur. Urol.*, 49:466–477, 2006. doi: 10.1016/j.eururo.2005.12.031.

[16] R. J. Sylvester, O. Rodríguez, V. Hernández, D. Turturica, L. Bauerová, et al. European Association of Urology (EAU) Prognostic Factor Risk Groups for Non–muscle-invasive Bladder Cancer (NMIBC) Incorporating the WHO 2004/2016 and WHO 1973 Classification Systems for Grade: An Update from the EAU NMIBC Guidelines Panel. *Eur. Urol.*, 79:480–488, 2021. doi: 10.1016/j.eururo.2020.12.033.

[17] T. Powles, J. Bellmunt, E. Comperat, M. De Santis, R. Huddart, et al. Bladder cancer: ESMO Clinical Practice Guideline for diagnosis, treatment and follow-up. *Ann. Oncol.*, 33:244–258, 2022. doi: 10.1016/j.annonc.2021.11.012.

[18] B. Li, Y.-P. Cao, X.-Q. Feng, and H. Gao. Surface wrinkling of mucosa induced by volumetric growth: Theory, simulation and experiment. *J. Mech. Phys. Solids*, 59:758–774, 2011. doi: 10.1016/j.jmps.2011.01.010.

[19] B. Li, Y.-P. Cao, X.-Q. Feng, and H. Gao. Mechanics of morphological instabilities and surface wrinkling in soft materials: a review. *Soft Matter*, 8:5728–5745, 2012. doi: 10.1039/C2SM00011C.

[20] F. Wu, J. Yang, J. Liu, Y. Wang, J. Mu, et al. Signaling pathways in cancer-associated fibroblasts and targeted therapy for cancer. *Signal Transduct. Target. Ther.*, 6:218, 2021.

[21] S. Brassart-Pasco, S. Brézillon, B. Brassart, L. Ramont, J.-B. Oudart, and J. C. Monboisse. Tumor Microenvironment: Extracellular Matrix Alterations Influence Tumor Progression. *Front. Oncol.*, 10, 2020. doi: 10.3389/fonc.2020.00397.

[22] H. Raskov, A. Orhan, S. Gaggar, and I. Gögenur. Cancer-Associated Fibroblasts and Tumor-Associated Macrophages in Cancer and Cancer Immunotherapy. *Front. Oncol.*, 11, 2021. doi: 10.3389/fonc.2021.668731.

[23] N. V. Popova and M. Jücker. The Functional Role of Extracellular Matrix Proteins in Cancer. *Cancers*, 14:238, 2022. doi: 10.3390/cancers14010238.

[24] E. Henke, R. Nandigama, and S. Ergün. Extracellular Matrix in the Tumor Microenvironment and Its Impact on Cancer Therapy. *Front. Mol. Biosci.*, 6, 2020. doi: 10.3389/fmolb.2019.00160.

[25] S. Banerjee, W.-C. Lo, P. Majumder, D. Roy, M. Ghorai, et al. Multiple roles for basement membrane proteins in cancer progression and EMT. *Eur. J. Cell Biol.*, 101:151220, 2022. doi: 10.1016/j.ejcb.2022.151220.

[26] R. G. Rowe and S. J. Weiss. Breaching the basement membrane: who, when and how? *Trends Cell Biol.*, 18: 560–574, 2008. doi: 10.1016/j.tcb.2008.08.007.

[27] J. Chang and O. Chaudhuri. Beyond proteases: Basement membrane mechanics and cancer invasion. *J. Cell Biol.*, 218:2456–2469, 2019. doi: 10.1083/jcb.201903066.

[28] J. Chang, A. Saraswathibhatla, Z. Song, S. Varma, C. Sanchez, et al. Cell volume expansion and local contractility drive collective invasion of the basement membrane in breast cancer. *Nat. Mater.*, 23:711–722, 2024. doi: 10.1038/s41563-023-01716-9.

[29] L. Chin, Y. Xia, D. E. Discher, and P. A. Janmey. Mechanotransduction in cancer. *Curr. Opin. Chem. Eng.*, 11:77–84, 2016. doi: 10.1016/j.coche.2016.01.011.

[30] J. M. Northcott, I. S. Dean, J. K. Mouw, and V. M. Weaver. Feeling Stress: The Mechanics of Cancer Progression and Aggression. *Front. Cell Dev. Biol.*, 6, 2018. doi: 10.3389/fcell.2018.00017.

[31] K. Nargess and M. Yanlan. To form and function: on the role of basement membrane mechanics in tissue development, homeostasis and disease. *Open Biol.*, 11:200360, 2021. doi: 10.1098/rsob.200360.

[32] G. S. van Tienderen, J. Conboy, I. Muntz, J. Willemse, J. Tieleman, et al. Tumor decellularization reveals proteomic and mechanical characteristics of the extracellular matrix of primary liver cancer. *Biomater. Adv.*, 146:213289, 2023. doi: 10.1016/j.bioadv.2023.213289.

[33] S. Huang and D. E. Ingber. Cell tension, matrix mechanics, and cancer development. *Cancer Cell*, 8:175–176, 2005. doi: 10.1016/j.ccr.2005.08.009.

[34] M. W. Pickup, J. K. Mouw, and V. M. Weaver. The extracellular matrix modulates the hallmarks of cancer. *EMBO Rep.*, 15:1243–1253, 2014. doi: 10.15252/embr.201439246.

[35] L. Martinez-Vidal, V. Murdica, C. Venegoni, F. Pederzoli, M. Bandini, et al. Causal contributors to tissue stiffness and clinical relevance in urology. *Commun. Biol.*, 4:1–16, 2021. doi: 10.1038/s42003-021-02539-7.

[36] H. Zhu, H. Chen, J. Wang, L. Zhou, and S. Liu. Collagen stiffness promoted non-muscle-invasive bladder cancer progression to muscle-invasive bladder cancer. *OncoTargets Ther.*, 12:3441–3457, 2019. doi: 10.2147/OTT.S194568.

[37] L. Conrad, S. V. M. Runser, H. Fernando Gómez, C. M. Lang, M. S. Dumond, et al. The biomechanical basis of biased epithelial tube elongation in lung and kidney development. *Development*, 148:dev194209, 2021. doi: 10.1242/dev.194209.

[38] A. Lopez-Beltran and R. Montironi. Non-invasive urothelial neoplasms: According to the most recent who classification. *Eur. Urol.*, 46:170–176, 2004. doi: https://doi.org/10.1016/j.eururo.2004.03.017.

[39] Z.Y. Huang, W. Hong, and Z. Suo. Nonlinear analyses of wrinkles in a film bonded to a compliant substrate. *J. Mech. Phys. Solids*, 53:2101–2118, 2005. doi: 10.1016/j.jmps.2005.03.007.

[40] E. Sultan and A. Boudaoud. The Buckling of a Swollen Thin Gel Layer Bound to a Compliant Substrate. *J. Appl. Mech.*, 75:051002, 2008. doi: 10.1115/1.2936922.

[41] B. Li, F. Jia, Y.-P. Cao, X.-Q. Feng, and H. Gao. Surface wrinkling patterns on a core-shell soft sphere. *Phys. Rev. Lett.*, 106:234301, 2011. doi: 10.1103/PhysRevLett.106.234301.

[42] F. Brau, P. Damman, H. Diamant, and T. A. Witten. Wrinkle to fold transition: influence of the substrate response. *Soft Matter*, 9:8177–8186, 2013. doi: 10.1039/C3SM50655J.

[43] Q. Wang and X. Zhao. Phase Diagrams of Instabilities in Compressed Film-Substrate Systems. *J. Appl. Mech.*, 81: 051004, 2013. doi: 10.1115/1.4025828.

[44] T. Tallinen, J. Y. Chung, J. S. Biggins, and L. Mahadevan. Gyrification from constrained cortical expansion. *Proc. Natl. Acad. Sci. U.S.A.*, 111:12667–12672, 2014. doi: 10.1073/pnas.1406015111.

[45] N. Stoop, R. Lagrange, D. Terwagne, P. M. Reis, and J. Dunkel. Curvature-induced symmetry breaking determines elastic surface patterns. *Nat. Mater.*, 14, 2015. doi: 10.1038/nmat4202.

[46] A. E. Shyer, T. Tallinen, N. L. Nerurkar, Z. Wei, E. S. Gil, et al. Villification: How the gut gets its villi. *Science*, 342: 212–218, 2013. doi: 10.1126/science.1238842.

[47] M. Ben Amar and F. Jia. Anisotropic growth shapes intestinal tissues during embryogenesis. *Proc. Natl. Acad. Sci. U.S.A.*, 110:10525–10530, 2013. doi: 10.1073/pnas.1217391110.

[48] L. Pocivavsek, R. Dellsy, A. Kern, S. Johnson, B. Lin, et al. Stress and Fold Localization in Thin Elastic Membranes. *Science*, 320:912–916, 2008. doi: 10.1126/science.1154069.

[49] F. Brau, H. Vandeparre, A. Sabbah, C. Poulard, A. Boudaoud, and P. Damman. Multiple-length-scale elastic instability mimics parametric resonance of nonlinear oscillators. *Nat. Phys.*, 7:56–60, 2010. doi: 10.1038/nphys1806.

[50] R. Zhao, T. Zhang, M. Diab, H. Gao, and K.-S. Kim. The primary bilayer ruga-phase diagram I: Localizations in ruga evolution. *Extreme Mech. Lett.*, 4:76–82, 2015. doi: 10.1016/j.eml.2015.04.006.

[51] S. P. Jost, J. A. Gosling, and J. S. Dixon. The morphology of normal human bladder urothelium. *J. Anat.*, 167:103–115, 1989.

[52] M. A. Biot. Folding instability of a layered viscoelastic medium under compression. *Proc. Roy. Soc. A*, 242:444–454, 1957. doi: 10.1098/rspa.1957.0187.

[53] J. Groenewold. Wrinkling of plates coupled with soft elastic media. *Phys. A: Stat. Mech. Appl.*, 298:32–45, 2001. doi: 10.1016/S0378-4371(01)00209-6.

[54] L. Martinez-Vidal, M. Chighizola, M. Berardi, E. Alchera, I. Locatelli, et al. Micro-mechanical fingerprints of the rat bladder change in actinic cystitis and tumor presence. *Commun. Biol.*, 6:1–12, 2023. doi: 10.1038/s42003-023-04572-0.

[55] C. Leclech, C. F. Natale, and A. I. Barakat. The basement membrane as a structured surface – role in vascular health and disease. *J. Cell Sci.*, 133, 2020. doi: 10.1242/jcs.239889.

[56] M. Lekka, P. Laidler, D. Gil, J. Lekki, Z. Stachura, and A. Z. Hrynkiewicz. Elasticity of normal and cancerous human bladder cells studied by scanning force microscopy. *Eur. Biophys. J.*, 28:312–316, 1999. doi: 10.1007/s002490050213.

[57] J. R. Ramos, J. Pabijan, R. Garcia, and M. Lekka. The softening of human bladder cancer cells happens at an early stage of the malignancy process. *Beilstein J. Nanotechnol.*, 5:447–457, 2014. doi: 10.3762/bjnano.5.52.

[58] N. Liu, M. Leng, T. Yue, L. Dong, Y. Liu, et al. Simultaneously Quantifying Both Young's Modulus and Specific Membrane Capacitance of Bladder Cancer Cells with Different Metastatic Potential. *Micromachines*, 11:249, 2020. doi: 10.3390/mi11030249.

[59] S. Monteiro-Reis, J. P. S. Ferreira, R. A. Pires, J. Lobo, J. A. Carvalho, et al. Bladder Wall Stiffness after Cystectomy in Bladder Cancer Patients: A Preliminary Study. *Cancers*, 15:359, 2023. doi: 10.3390/cancers15020359.

[60] X. Z. Huang, A. Y. Zhou, M. W. Liu, Y. Zhang, and P. Xu. Shear Wave Elasticity Differentiation Between Low- and High-Grade Bladder Urothelial Carcinoma and Correlation With Collagen Fiber Content. *J. Ultrasound Med.*, 40: 113–122, 2021. doi: 10.1002/jum.15381.

[61] H. Ghasemi, S. H. Mousavibahar, M. Hashemnia, J. Karimi, I. Khodadadi, et al. Tissue stiffness contributes to YAP activation in bladder cancer patients undergoing transurethral resection. *Ann. N. Y. Acad. Sci*, 1473:48–61, 2020. doi: 10.1111/nyas.14358.

[62] V. Cristini, H. B. Frieboes, R. Gatenby, S. Caserta, M. Ferrari, and J. Sinek. Morphologic Instability and Cancer Invasion. *Clin. Cancer Res.*, 11:6772–6779, 2005. doi: 10.1158/1078-0432.CCR-05-0852.

[63] P. Ciarletta. Buckling Instability in Growing Tumor Spheroids. *Phys. Rev. Lett.*, 110:158102, 2013. doi: 10.1103/PhysRevLett.110.158102.

[64] P. Katira, R. Bonnecaze, and M. Zaman. Modeling the Mechanics of Cancer: Effect of Changes in Cellular and Extra-Cellular Mechanical Properties. *Front. Oncol.*, 3:145, 2013. doi: 10.3389/fonc.2013.00145.

[65] T. Stylianopoulos. The Solid Mechanics of Cancer and Strategies for Improved Therapy. *J. Biomech. Eng.*, 139: 021004, 2017. doi: 10.1115/1.4034991.

[66] D. H. Ewalt, P. S. Howard, B. Blyth, H. M. Snyder, J. W. Duckett, et al. Is Lamina Propria Matrix Responsible for Normal Bladder Compliance? *J. Urol.*, 148:544–549, 1992. doi: 10.1016/S0022-5347(17)36650-8.

[67] B. Davies, J. Waxman, H. Wasan, P. Abel, G. Williams, et al. Levels of Matrix Metalloproteases in Bladder Cancer Correlate with Tumor Grade and Invasion. *Cancer Res.*, 53:5365–5369, 1993.

[68] G. Elayat, I. Punev, and A. Selim. An Overview of Angiogenesis in Bladder Cancer. *Curr. Oncol. Rep.*, 2023. doi: 10.1007/s11912-023-01421-5.

[69] R. N. Miftahof and H. G. Nam. The Bladder as a Dynamic System. In Roustem N. Miftahof and Hong Gil Nam, editors, *Biomechanics of the Human Urinary Bladder*, pages 1–23. Springer, 2013. doi: 10.1007/978-3-642-36146-3_1.

[70] S. F. Shariat, M. Milowsky, and M. J. Droller. Bladder cancer in the elderly. *Urol. Oncol. Semin. Orig. Investig.*, 27:653–667, 2009. doi: 10.1016/j.urolonc.2009.07.020.

[71] R. S. Barsoum. Urinary Schistosomiasis: Review. *J. Adv. Res.*, 4:453–459, 2013. doi: 10.1016/j.jare.2012.08.004.

[72] F. Suriano, E. Altobelli, F. Sergi, and M. Buscarini. Bladder Cancer After Radiotherapy for Prostate Cancer. *Rev. Urol.*, 15:108–112, 2013.

[73] M. Moschini, E. Zaffuto, P. I. Karakiewicz, D. D. Andrea, B. Foerster, et al. External Beam Radiotherapy Increases the Risk of Bladder Cancer When Compared with Radical Prostatectomy in Patients Affected by Prostate Cancer: A Population-based Analysis. *Eur. Urol.*, 75:319–328, 2019. doi: 10.1016/j.eururo.2018.09.034.

[74] S. E. Martin, E. M. Begun, E. Samir, M. T. Azaiza, S. Allegro, and M. Abdelhady. Incidence and Morbidity of Radiation-Induced Hemorrhagic Cystitis in Prostate Cancer. *Urology*, 131:190–195, 2019. doi: 10.1016/j.urology.2019.05.034.

[75] B. W. G. van Rhijn, M. Burger, Y. Lotan, E. Solsona, C. G. Stief, et al. Recurrence and Progression of Disease in Non–Muscle-Invasive Bladder Cancer: From Epidemiology to Treatment Strategy. *Eur. Urol.*, 56:430–442, 2009. doi: 10.1016/j.eururo.2009.06.028.

[76] K. Saginala, A. Barsouk, J. S. Aluru, P. Rawla, S. A. Padala, and A. Barsouk. Epidemiology of Bladder Cancer. *Med. Sci.*, 8:15, 2020. doi: 10.3390/medsci8010015.

[77] X. Hu, G. Li, and S. Wu. Advances in Diagnosis and Therapy for Bladder Cancer. *Cancers*, 14:3181, 2022. doi: 10.3390/cancers14133181.

[78] A. Stylianou, M. Lekka, and T. Stylianopoulos. AFM assessing of nanomechanical fingerprints for cancer early diagnosis and classification: from single cell to tissue level. *Nanoscale*, 10:20930–20945, 2018. doi: 10.1039/C8NR06146G.

[79] Z. He, W. Kosinska, Z.-L. Zhao, X.-R. Wu, and J. B. Guttenplan. Tissue-specific mutagenesis by N-butyl-N-(4-hydroxybutyl)nitrosamine as the basis for urothelial carcinogenesis. *Mutat. Res. Genet. Toxicol. Environ. Mutagen.*, 742:92–95, 2012. doi: 10.1016/j.mrgentox.2011.11.015.

[80] M. Degoricija, J. Korac-Prlic, K. Vilovic, T. Ivanisevic, B. Haupt, et al. The dynamics of the inflammatory response during BBN-induced bladder carcinogenesis in

mice. *J. Transl. Med.*, 17:394, 2019. doi: 10.1186/s12967-019-02146-5.

[81] E. A. Susaki, K. Tainaka, D. Perrin, H. Yukinaga, A. Kuno, and H. R. Ueda. Advanced CUBIC protocols for whole-brain and whole-body clearing and imaging. *Nat. Protoc.*, 10:1709–1727, 2015. doi: 10.1038/nprot.2015.085.

[82] J. Schindelin, I. Arganda-Carreras, E. Frise, V. Kaynig, M. Longair, et al. Fiji: an open-source platform for biological-image analysis. *Nat. Methods*, 9:676–682, 2012. doi: 10.1038/nmeth.2019.

[83] D. Hörl, F. Rojas Rusak, F. Preusser, P. Tillberg, N. Randel, et al. BigStitcher: reconstructing high-resolution image datasets of cleared and expanded samples. *Nat. Methods*, 16:870–874, 2019. doi: 10.1038/s41592-019-0501-0.

[84] S. Berg, D. Kutra, T. Kroeger, C. N. Straehle, B. X. Kausler, et al. ilastik: interactive machine learning for (bio)image analysis. *Nat. Methods*, 16:1226–1232, 2019. doi: 10.1038/s41592-019-0582-9.

[85] P. Cignoni, M. Callieri, M. Corsini, M. Dellepiane, F. Ganovelli, and G. Ranzuglia. *MeshLab: an Open-Source Mesh Processing Tool*. The Eurographics Association, 2008. doi: 10.2312/LocalChapterEvents/ItalChap/ItalianChapConf2008/129-136.

[86] M. Kazhdan and H. Hoppe. Screened Poisson surface reconstruction. *ACM Trans. Graph.*, 32:1–13, 2013. doi: 10.1145/2487228.2487237.

[87] N. Sofroniew, T. Lambert, K. Evans, J. Nunez-Iglesias, G. Bokota, et al. napari: a multi-dimensional image viewer for Python, 2022. `https://10.5281/zenodo.7276432`.

[88] A. Wolny, L. Cerrone, A. Vijayan, R. Tofanelli, A. V. Barro, et al. Accurate and versatile 3d segmentation of plant tissues at cellular resolution. *eLife*, 9:e57613, 2020. doi: 10.7554/eLife.57613.

[89] K. Yamauchi, R. Haase, and Sobolewski P. morphometrics/morphometrics: v0.0.9, 2023. `https://doi.org/10.5281/zenodo.8256767`.

[90] Blender Online Community. *Blender - a 3D modelling and rendering package*. Blender Foundation, Stichting Blender Foundation, Amsterdam, 2018. URL `http://www.blender.org`.

[91] J. C. Simo and Thomas J. R. Hughes. *Computational inelasticity*, volume 7 of *Interdisciplinary applied mathematics*. Springer, New York, 1998. ISBN 978-0-387-97520-7. doi: 10.1007/b98904.

[92] D. J. Rosario, G. C. Reilly, E. Ali Salah, M. Glover, A. J. Bullock, and S. Macneil. Decellularization and sterilization of porcine urinary bladder matrix for tissue engineering in the lower urinary tract. *Regen. Med.*, 3:145–156, 2008. doi: 10.2217/17460751.3.2.145.

[93] S. Sabetkish, N. Sabetkish, and A.-M. Kajbafzadeh. In-vivo regeneration of bladder muscular wall with whole decellularized bladder matrix: A novel hourglass technique for duplication of bladder volume in rabbit model. *J. Pediatr. Surg.*, 55:2226–2232, 2020. doi: 10.1016/j.jpedsurg.2019.11.020.

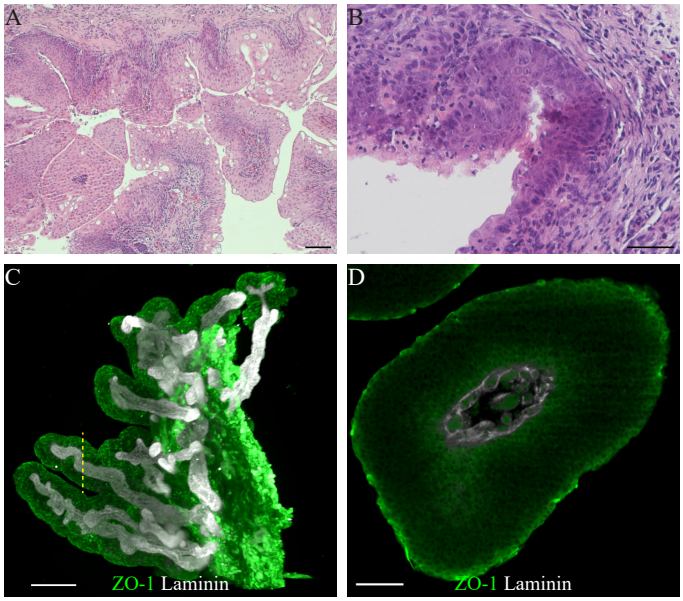

Extended Data Figure 1: Bladder tumors in mice and humans. (A) Low-grade papillary tumor in the mouse bladder 11 weeks post BBN, scale bar: 100 µm, (B) CIS in the mouse bladder 8 weeks post BBN. Scale bar: 50 µm. (C) Human papillary tumor. Yellow dotted line: approximate position of (D). Scale bar: 500 µm. (D) Digital cut thru human papilla. Scale bar: 100 µm. All images show individual exemplars, not repeated experiments.

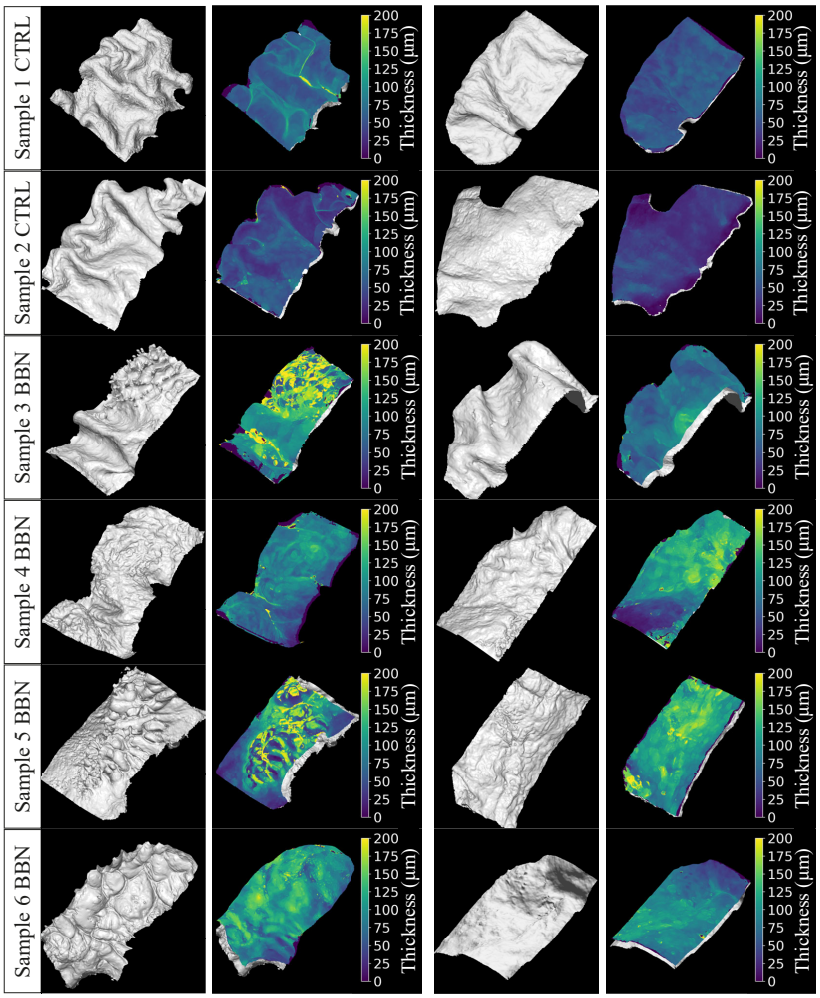

Extended Data Figure 2: Examples of different thickness measurements in mice. Comparison of different degrees of BM alterations and thickening in mouse biopsies from six different bladders, two tissue samples from each bladder.

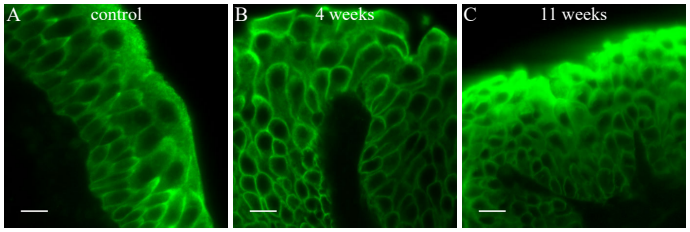

Extended Data Figure 3: 2D slices from SPIM images of sample 2 analyzed in Fig. 3. (A) Control. (B) BBN treated mice 4 weeks post BBN. (C) BBN treated mice 11 weeks post BBN. Scale bars: 20 µm.

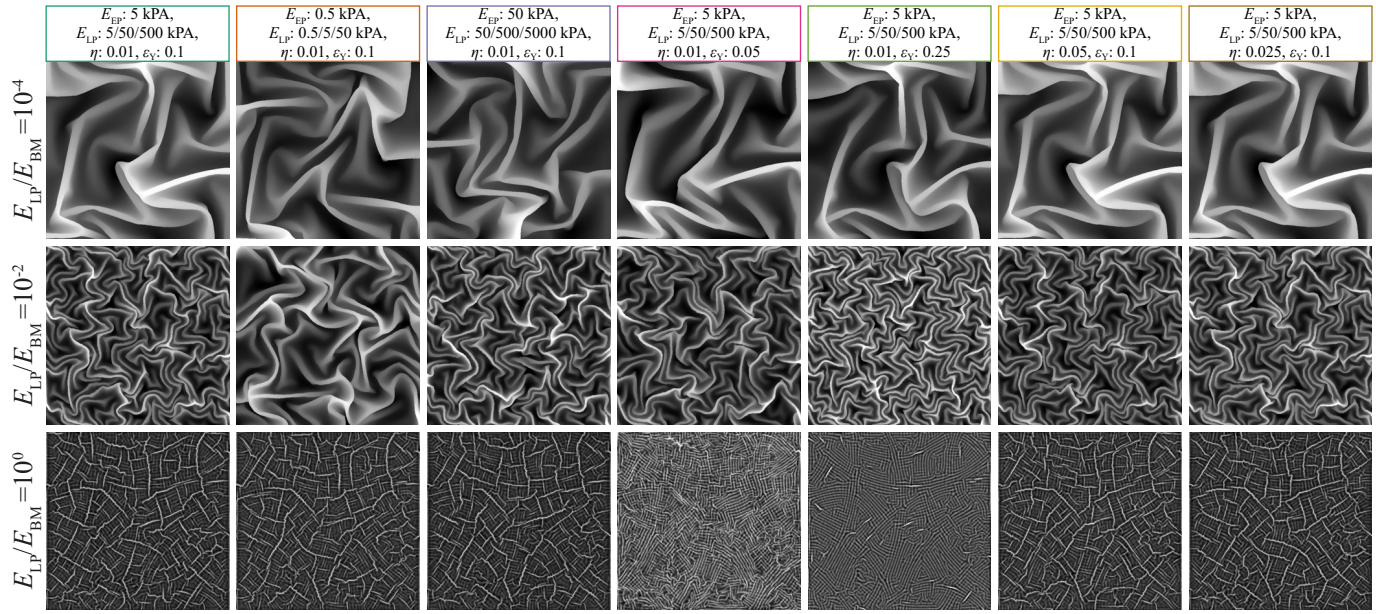

Extended Data Figure 4: Simulated BM height maps. Overview of all observed BM height profiles from the simulations in Fig. 4C with individually normalized contrast. The box colors correspond to the colors of the data points in the plot.

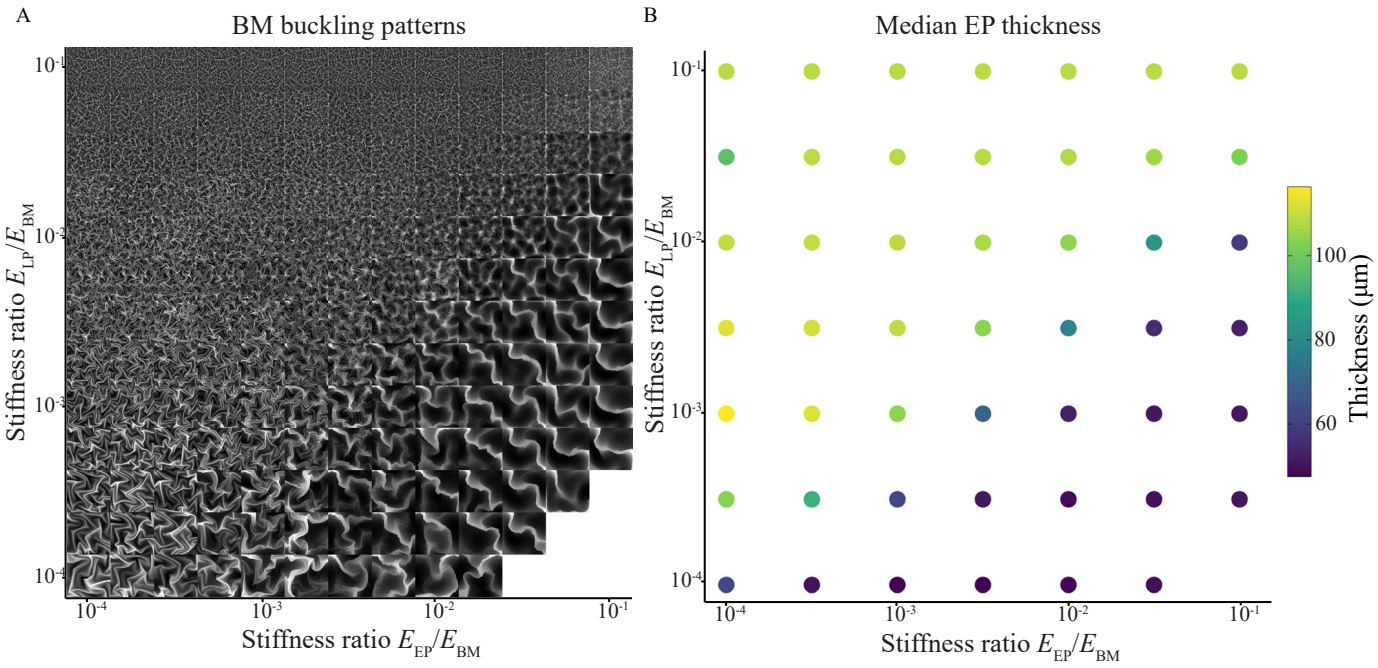

Extended Data Figure 5: Simulated BM height maps and EP thickness. (A) Overview of all observed BM height profiles from the simulations in Fig. 5D with individually normalized contrast. (B) Overview of a subset of thickness measurements from the simulations in Fig. 5D.

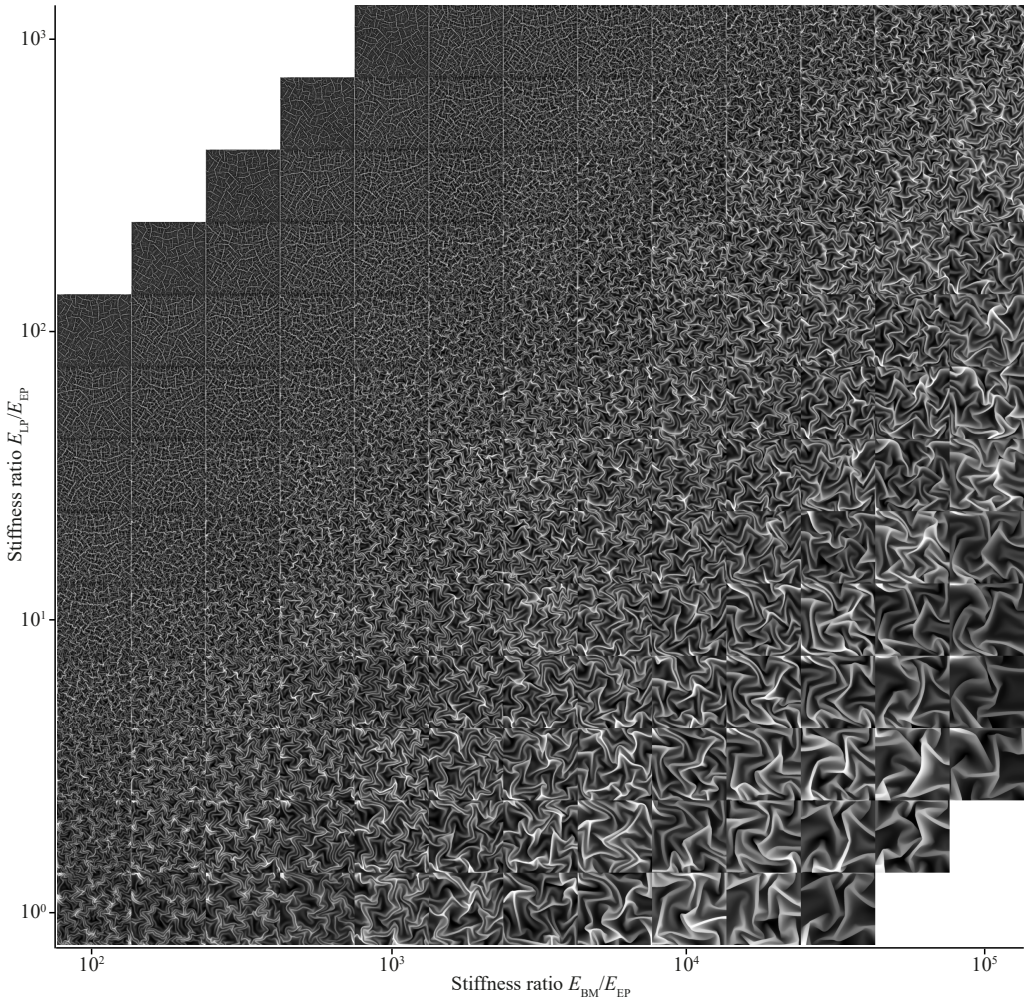

Extended Data Figure 6: Simulated BM height maps. Overview of all observed BM height profiles from the simulations in Fig. 5E with individually normalized contrast.

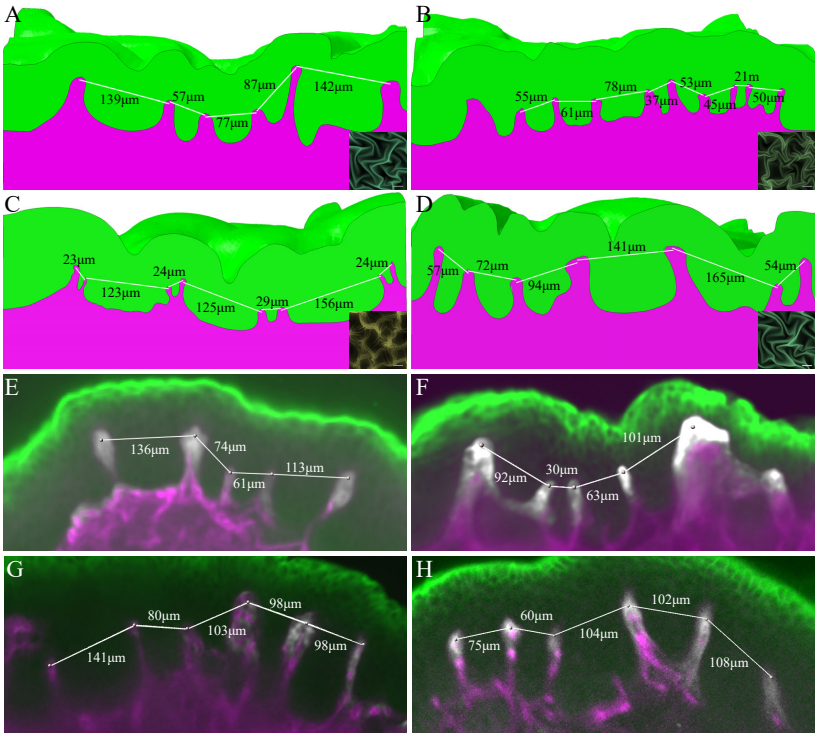

Extended Data Figure 7: Quantification of papillary distances in vertical slices through the mucosa. (A–D) Numerical simulations. Insets show corresponding BM height profiles from Fig. 5. (E–H) BBN-treated mice, 4 weeks (E) and 6 weeks (F–H) after BBN stop, with the urothelium marked in green, the vasculature in the lamina propria in purple and the basement membrane in white. Beeline distances between adjacent tips are indicated.

Contents

Supplementary Tables

Supplementary Table 1: Measured cell morphometrics. Number of cells n, mean, median and standard deviation (sd) for the morphometric quantification displayed in Fig. 3D–G.

		Area (µm^2)			Volume (µm^3)			Elongation			Sphericity		
Sample	n	mean	median	sd	mean	median	sd	mean	median	sd	mean	median	sd
Control S1	356	954	807	424	2160	1596	1508	2.33	2.26	0.51	0.82	0.83	0.04
Control S2	388	1034	913	469	2300	1789	1571	3.02	2.91	0.80	0.79	0.80	0.05
4 weeks S1	265	1043	811	633	2595	1696	2607	2.07	1.99	0.49	0.83	0.83	0.04
4 weeks S2	529	1280	1202	517	3109	2819	1641	2.43	2.24	0.77	0.80	0.80	0.06
11 weeks S1	337	1064	967	500	2478	2028	1763	2.22	2.14	0.50	0.81	0.81	0.04
11 weeks S2	417	714	673	221	1379	1259	605	1.87	1.83	0.38	0.83	0.83	0.04

Supplementary Table 2: Statistics of the differences in cell morphometrics. Exact adjusted P values from Pairwise Wilcoxon test with Bonferroni correction for multiple testing, and Wilcoxon effect size r corresponding to the significance levels and effect sizes indicated in Fig. 3I.

		Area		Volume		Elongation		Sphericity	
Sample 1	Sample 2	adj. P value	r	adj. P value	r	adj. P value	r	adj. P value	r
Control S1	Control S2	3.09×10^{-1}	0.08	1	0.02	1.80×10^{-37}	0.48	3.12×10^{-26}	0.40
Control S1	4 weeks S1	1	0.01	1	0.03	8.43×10^{-11}	0.28	2.50×10^{-1}	0.10
Control S1	4 weeks S2	4.04×10^{-24}	0.35	4.46×10^{-24}	0.35	1	0.01	1.95×10^{-11}	0.24
Control S1	11 weeks S1	9.56×10^{-4}	0.15	3.00×10^{-3}	0.14	1.60×10^{-2}	0.12	2.49×10^{-5}	0.18
Control S1	11 weeks S2	3.14×10^{-21}	0.35	8.02×10^{-22}	0.36	1.07×10^{-37}	0.47	1.06×10^{-1}	0.10
Control S2	4 weeks S1	1	0.06	1	0.01	1.10×10^{-56}	0.63	4.88×10^{-28}	0.44
Control S2	4 weeks S2	6.39×10^{-14}	0.26	1.23×10^{-17}	0.29	1.77×10^{-32}	0.40	3.20×10^{-2}	0.10
Control S2	11 weeks S1	1	0.05	2.40×10^{-1}	0.09	1.16×10^{-48}	0.55	3.46×10^{-8}	0.22
Control S2	11 weeks S2	3.12×10^{-28}	0.40	4.22×10^{-21}	0.34	1.71×10^{-97}	0.74	9.69×10^{-39}	0.47
4 weeks S1	4 weeks S2	1.06×10^{-14}	0.29	2.97×10^{-13}	0.27	4.27×10^{-10}	0.24	4.11×10^{-15}	0.29
4 weeks S1	11 weeks S1	8.30×10^{-2}	0.11	4.35×10^{-1}	0.09	9.10×10^{-4}	0.16	1.03×10^{-8}	0.25
4 weeks S1	11 weeks S2	1.43×10^{-15}	0.32	2.21×10^{-17}	0.34	7.90×10^{-7}	0.21	1	0.01
4 weeks S2	11 weeks S1	3.61×10^{-10}	0.23	2.02×10^{-10}	0.23	2.50×10^{-2}	0.11	1.02×10^{-1}	0.09
4 weeks S2	11 weeks S2	9.87×10^{-74}	0.60	7.76×10^{-76}	0.60	9.84×10^{-38}	0.42	5.66×10^{-21}	0.31
11 weeks S1	11 weeks S2	1.66×10^{-32}	0.44	5.22×10^{-32}	0.44	7.53×10^{-23}	0.37	7.68×10^{-12}	0.26

Supplementary Table 3: Simulation parameters. Overview of all parameters from the simulations displayed in Fig. 4C.

		Young's modulus E (kPa)			Hardening η		Yield strain ϵ_Y	
Simulation	E_{LP}/E_{BM}	EP	LP	BM	EP	LP	EP	LP
1	10^{-4}	5	5	50000	0.01	0.01	0.1	0.1
	10^{-2}	5	50	5000	0.01	0.01	0.1	0.1
	10^{0}	5	500	500	0.01	0.01	0.1	0.1
2	10^{-4}	0.5	0.5	5000	0.01	0.01	0.1	0.1
	10^{-2}	0.5	5	500	0.01	0.01	0.1	0.1
	10^{0}	0.5	50	50	0.01	0.01	0.1	0.1
3	10^{-4}	50	50	500000	0.01	0.01	0.1	0.1
	10^{-2}	50	500	50000	0.01	0.01	0.1	0.1
	10^{0}	50	5000	5000	0.01	0.01	0.1	0.1
4*	10^{-4}	5	5	50000	0.01	0.01	0.05	0.05
	10^{-2}	5	50	5000	0.01	0.01	0.05	0.05
	10^{0}	5	500	500	0.01	0.01	0.05	0.05
5	10^{-4}	5	5	50000	0.01	0.01	0.25	0.25
	10^{-2}	5	50	5000	0.01	0.01	0.25	0.25
	10^{0}	5	500	500	0.01	0.01	0.25	0.25
6	10^{-4}	5	5	50000	0.05	0.05	0.1	0.1
	10^{-2}	5	50	5000	0.05	0.05	0.1	0.1
	10^{0}	5	500	500	0.05	0.05	0.1	0.1
7	10^{-4}	5	5	50000	0.025	0.025	0.1	0.1
	10^{-2}	5	50	5000	0.025	0.025	0.1	0.1
	10^{0}	5	500	500	0.025	0.025	0.1	0.1

*Parameters used in the simulations displayed in Fig. 4D–F.

Supplementary Table 4: Measured stiffness of the BM. Mean Young's modulus at each measured position and mean Young's modulus over all positions, based on treatment group. n: number of measurements taken per position. P values corresponding to the significance levels indicated in Fig. 6B. Pairwise two-sided t-test with Bonferroni correction for multiple testing.

				Young's modulus E (kPa)		adjusted P value	
Animal	Condition	Position	n	mean	sd	Position 1	Position 2
1	BBN	1	20	46	27	—	—
		2	37	100	47	7.42×10^{-4}	—
		3	32	133	32	3.30×10^{-10}	3.10×10^{-1}
2	BBN	1	31	20	8	—	—
		2	43	121	44	2.37×10^{-20}	—
		3	39	125	50	4.46×10^{-21}	1
3	BBN	1	79	110	55	—	—
		2	41	147	59	1.38×10^{-3}	—
4	BBN	2	32	27	18	—	—
		3	39	77	30	—	1.94×10^{-4}
5	CTRL	1	44	136	47	—	—
		2	42	139	39	1	—
		3	40	104	37	1.38×10^{-1}	4.42×10^{-2}
6	CTRL	1	42	99	37	—	—
		2	38	126	50	7.67×10^{-1}	—
		3	46	120	40	1	1
7	CTRL	1	51	114	37	—	—
		2	48	139	53	6.52×10^{-1}	—
		3	46	101	31	1	2.67×10^{-3}
1–4	BBN	all	393	97	57		
5–7	CTRL	all	397	120	44		

Supplementary Table 5: Overview of animals used in this study. n: number of animals bred in total. Not all animals listed here were used for experiments and quantifications; individual numbers are specified in legends of the figures presenting the data.

			Group		
Experiment	weeks post BBN	n	BBN	CTRL	Comment
Establishing treatment timeline	2–11	16	16	0	4 mice each at 2, 5, 7 and 11 weeks
Histopathology 11 weeks	11	—	—	—	from 11 week sampling point timeline establishing
Histopathology 4 weeks	4	4	2	2	Additional H&E staining were obtained from spare material from mice used for SPIM imaging at 4 weeks
SPIM imaging 11 weeks	11	20	10	10	Control cohort samples for cellular segmentation were obtained from week 11 CTRL group
SPIM & live imaging 6 weeks	6	12	8	4	For manual distance quantification in ED Fig. 7 and live imaging (Supplementary Note 1)
SPIM imaging 4 weeks	4	39	22	17	
AFM	4	7	4	3	
Total	2–11	98	62	36	

Supplementary Note 1: Long-term life culturing of bladder tissue

We set up a long-term culture experiment using a customized sample holder system with the intent to monitor the outgrowth of papilla and changes in the buckling structure of the BM *ex vivo*. However, the system was not suited for the intended purpose, because lack of blood supply leads to a flattening of the BM to the degree that the vasculature retracts, as the vasculature that maintains the papilla is no longer nurtured (Supplementary Fig. 1). The additional methods for the live culturing system are detailed in Supplementary Note 2.

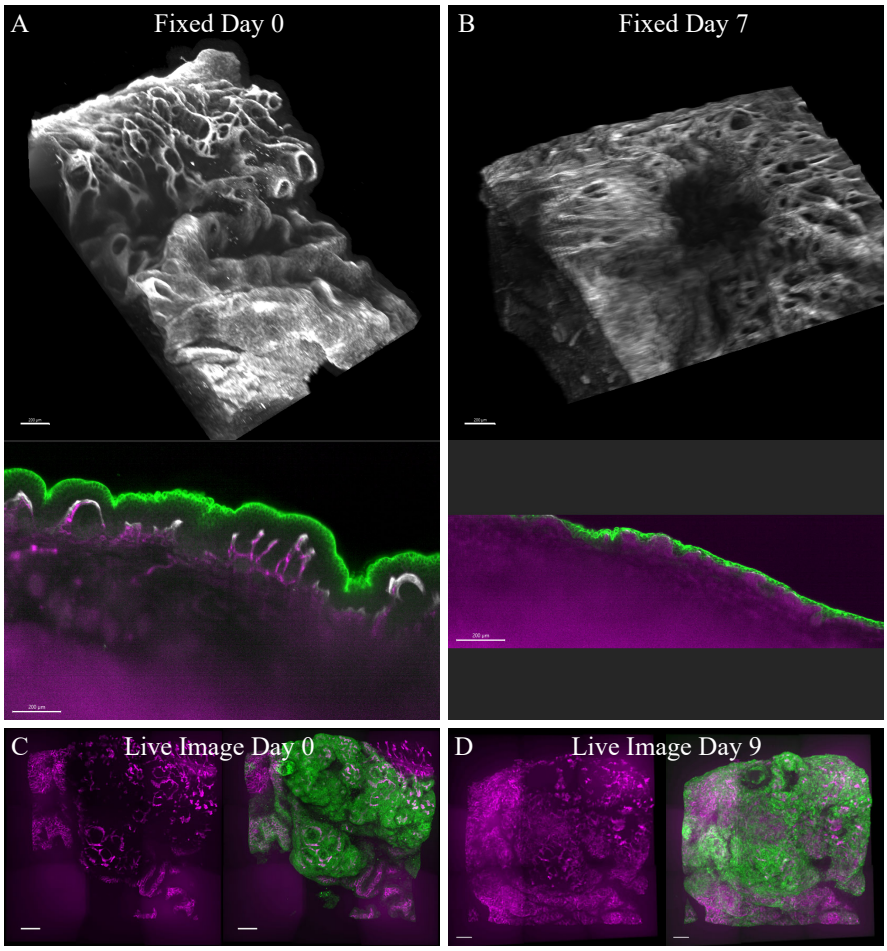

Supplementary Figure 1: Flattening of the BM during live imaging of bladder tissue explants. (A,B) 3D view of a bladder lesion in a BBN-treated mouse (top) and 2D cut through the same lesion (bottom), at day 0 (A) and 7 (B) in an *ex vivo* culture, both obtained from the same mouse bladder. (C,D) Top view on a lesion in a BBN-treated mouse bladder at day 0 (C) and day 9 (D) of a life culture illustrating the partial retraction of the vasculature and the flattening of the urothelium. Green: urothelium, magenta: vasculature, lamina propria and muscle tissue, white: basement membrane. Scale bars: 200 µm.

Supplementary Note 2: Supplementary Methods

Sample holder preparation

The sample holder system consisted of a modified cell strainer and a silicon elastomer-filled pan to fix it. The modified cell strainers (40 µm pore size (Corning)), which served as sample holders, were created by removing the top part of the cell strainer and the mesh on the side to create four legs. The 3D-printed flat pan was filled with a silicone elastomer (SYLGARD 184 silicon) and before the elastomer was cured, a 3D-printed stamp was placed into the pan to create four grooves shaped such that the legs of a modified cell strainer fit tightly into them in the elastomer and were thus held in place. The mesh files for 3D printing of the sample pan and stamp are available in the git repository (see Code Availability). Before mounting the tissue samples, all components of the sample holder system were placed for 1 h under the UV lamp of a sterile work bench for disinfection.

Tissue culture medium preparation

The tissue culture medium was based on the protocol described in [1]. For tissue maintenance, the medium consisted of a 1:1 mix of MCDB153 medium (Sigma), supplemented with 1.18 $\mathrm{g\,L^{-1}}$ sodium bicarbonate (Gibco) and Advanced-DMEM (Gibco). The mixed medium was further supplemented with 15 $\mathrm{\mu g\,mL^{-1}}$ adenine (Sigma), 0.5 $\mathrm{\mu g\,mL^{-1}}$ hydrocortisone (Sigma), 0.1 $\mathrm{mmol\,L^{-1}}$ ethanolamine (Sigma), 0.1 $\mathrm{mmol\,L^{-1}}$ phosphoethanolamine (Sigma), 5 $\mathrm{\mu g\,mL^{-1}}$ insulin (Sigma), 1× penicillin/streptomycin (Gibco). For imaging, a phenol-red reduced medium was used, where the Advanced-DMEM medium was replaced with the phenol-red free Opti-MEM medium (Gibco).

Preparation of submerged cultures

For the live cultures, BBN treated mice were sacrificed 6 weeks after BBN stop and the bladders were immediately harvested and washed in cold DPBS (Gibco). Excess fatty tissue was removed with surgical scissors and forceps before cutting the bladders sagittally into halves. Bladder halves were further cut into approximately 5×5 mm specimens. The bladder pieces were then fixed on the outside of the bottom of the modified cell strainer with the urothelium facing outward, using a surgical polyamide suture (Serag-Wiessner). The cell strainer with the tissue was then pushed into the pan with the silicon elastomer. The assembled sample holder was subsequently placed in a 6-well plate and covered with approximately 6 mL of the above-described tissue maintenance medium. The culture plates were placed in a humidified incubator at 37°C and 5% CO_2 and the medium was exchanged every 2–3 days.

Live imaging

For imaging, the whole sample holder was transferred to a 35 mm Petri dish and covered with fresh phenol-red reduced medium. Manual time-laps imaging of the submerged cultures was performed on a Nikon N*i*-E upright confocal microscope featuring a Yokogawa CSU-W1 or CSU-X1 spinning disk unit (50 µm pinhole size) using a 16×/0.8 dipping objective with a 3 mm working distance (Nikon) and the NIS-Elements software version 5.30.05 (Nikon). The microscope was equipped with an environmental chamber for humidity, temperature and CO_2 control. Tiled acquisition was used to image a bigger section of the samples. After image acquisition, the sample holder was placed back into a 6-well plate with fresh tissue culture medium. Images of the live cultures were obtained every 3 days.

Endpoint imaging

3D image stacks of the fixed end-point samples were acquired using a Zeiss Lightsheet Z.1 SPIM. Tissue clearing, staining and image processing were performed as described in the main manuscript.

Supplementary Note 3: Elastic theory of wrinkling in multilayered tissues

In the computer simulations, we observed a transition between two morphologically distinct regimes of folding and wrinkling in the three-layer mucosa (Fig. 5D and 2A), depending on the relative stiffness of the epithelium (EP) and lamina propria (LP). If the passively deforming LP is much stiffer than the expanding EP ($E_{\mathrm{EP}} \ll E_{\mathrm{LP}}$) but softer than the basement membrane (BM), it is the BM alone that buckles and folds in between the EP and LP, which then act as compliant media for the BM, a regime we term "medium-like" deformation (Fig. 5D, upper left inset, and Supplementary Fig. 2B). For a considerably stiffer EP ($E_{\mathrm{EP}} \gg E_{\mathrm{LP}}$), on the other hand, the EP deforms together with the BM like an expanding stiff plate on a compliant substrate, a regime we term "plate-like" deformation (Fig. 5D, lower right inset, and Supplementary Fig. 2C). We propose that these two regimes and the transition between them provide a mechanical basis for structural changes in the mucosa that could be linked with the onset of bladder cancer formation through changes is tissue stiffness or thickness.

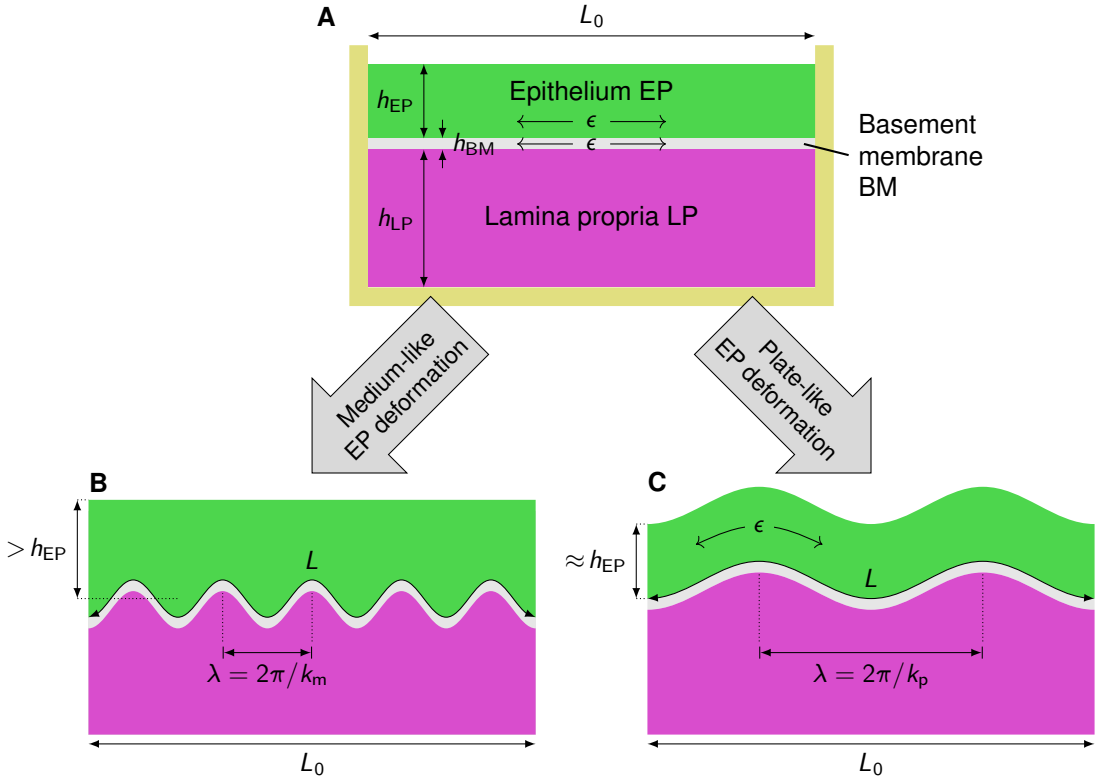

Supplementary Figure 2: Elastic theory of mucosa folding morphologies in 2D cross sections. **A** Initial, flat, unstressed configuration of the mucosa, represented by a three-layer elastic continuum. The epithelium (EP) and the basement membrane (BM) are assumed to expand in plane, the lamina propria (LP) is not. **B** In "medium-like" deformation, the EP acts like an elastic medium similarly to the LP, sandwiching the thin BM, which folds between them upon expansion. The BM buckles and folds with wavelength $\lambda = 2\pi/k_{\mathrm{m}}$, as it cannot expand horizontally, straining the EP and LP vertically. If the EP overgrows in parallel to the BM and is also prevented from horizontal expansion, it thickens vertically. **C** In "plate-like" deformation, the EP buckles together with the BM like a composite plate on an elastic substrate, the LP. Since the wavelength $\lambda = 2\pi/k_{\mathrm{p}}$ is proportional to the plate thickness, it is larger than in medium-like deformation. The undulating EP can attain its expanded length L with lower horizontal compression, and therefore does not thicken substantially.

The existence of two regimes can be understood from the stability theory of elastic layered structures, which goes back to the pioneering work of Biot [2]. Here, we derive the boundary separating them (Fig. 5D,E, black dashed line) analytically. Consider a 2D vertical cross section of the mucosa, and its small-deformation buckling behavior upon differential expansion. The EP, BM and LP layers are assumed to have unstrained initial thicknesses h_{EP}, h_{BM} and h_{LP}, Young's moduli E_{EP}, E_{BM} and E_{LP}, and Poisson ratios ν_{EP}, ν_{BM} and ν_{LP}, with $h_{\mathrm{BM}} \ll h_{\mathrm{EP}}, h_{\mathrm{LP}}$ and $E_{\mathrm{BM}} \gg E_{\mathrm{EP}}, E_{\mathrm{LP}}$ (Supplementary Fig. 2A). The EP and BM are assumed to expand horizontally by a volumetric growth strain $\epsilon > 0$, caused by proliferation of the epithelial cells and the membrane at the onset of cancer formation, for example.

We first consider the buckling of the thin and relatively stiff layer in between, the BM, and describe its vertical displacement by the field w. When the Euler buckling threshold is exceeded, it undulates harmonically

according to

$$w(x) = w_0 \sin(kx + \phi) \tag{1}$$

where ϕ is a phase angle that is irrelevant here (and is henceforth dropped), w_0 the compression-dependent amplitude, and $k = 2\pi/\lambda$ the wavenumber corresponding to wavelength λ. The arc length of the BM cross section over a certain number of wrinkles, n, is

$$L = \int_0^{n\lambda} \sqrt{1 + w'(x)^2}\, dx = \int_0^{2\pi n/k} \sqrt{1 + k^2 w_0^2 \cos^2(x)}\, dx. \tag{2}$$

For small deformations, the binomial approximation can be used to write

$$L \approx \int_0^{2\pi n/k} \left(1 + \frac{1}{2} k^2 w_0^2 \cos^2(x)\right) dx = \frac{2\pi n}{k} + \frac{\pi n}{2} k w_0^2. \tag{3}$$

This length arises from an original length $L_0 = 2\pi n/k$ strained by the Cauchy strain $\epsilon = \Delta L/L_0$ (Supplementary Fig. 2):

$$L = L_0 + \Delta L = \frac{2\pi n}{k}(1 + \epsilon) \quad \text{for} \quad \epsilon \approx \frac{k^2 w_0^2}{4}. \tag{4}$$

Using the latter relationship, the BM shape can be expressed in terms of the strain ϵ and the wavenumber k as

$$w(x) = \frac{2\sqrt{\epsilon}}{k} \sin(kx). \tag{5}$$

While ϵ is a free variable that reflects the amount of tissue expansion, the wavenumber is set through energy minimization. For the BM as a free elastic thin plate alone, this would be the bending energy, leading to a minimization of k (maximization of the wavelength λ). In a multi-layered structure, however, additional energy terms need to be considered that account for the deformation of the adjacent layers, which yields a different ground state wavelength for a given ϵ.

Considering, for now, the two-layer system composed of the BM and LP without EP, there are two main energy contributions: The bending of the thin BM, and the vertical displacement of the substrate (LP). As derived in [3], the corresponding energy densities under the plane strain assumption read

$$U_{\mathrm{LP}} = \frac{E_{\mathrm{LP}}(1 - \nu_{\mathrm{LP}})}{2(1 + \nu_{\mathrm{LP}})(3 - 4\nu_{\mathrm{LP}})} w_{0,\mathrm{LP}}^2\, k_{\mathrm{LP}} \qquad \text{and} \qquad U_{\mathrm{BM}} = \frac{E_{\mathrm{BM}} h_{\mathrm{BM}}^3}{48(1 - \nu_{\mathrm{BM}}^2)} w_{0,\mathrm{BM}}^2\, k_{\mathrm{BM}}^4. \tag{6}$$

Since the substrate and the plate deform together with the same amplitude and wavenumber, the same relationship $\epsilon \approx k^2 w_0^2/4$ holds for both the LP and the BM, with $w_{0,\mathrm{LP}} = w_{0,\mathrm{BM}} =: w_0$ and $k_{\mathrm{LP}} = k_{\mathrm{BM}} =: k$. Thus, one can eliminate the amplitude and write the total energy density in terms of the strain ϵ that produces this undulation:

$$U = U_{\mathrm{LP}} + U_{\mathrm{BM}} = \frac{\epsilon}{3} \left(\frac{6 E_{\mathrm{LP}}(1 - \nu_{\mathrm{LP}})}{k(1 + \nu_{\mathrm{LP}})(3 - 4\nu_{\mathrm{LP}})} + \frac{E_{\mathrm{BM}} h_{\mathrm{BM}}^3 k^2}{4(1 - \nu_{\mathrm{BM}}^2)} \right) \tag{7}$$

Minimizing the energy ($dU/dk = 0$) yields the classical elastic ground state wavenumber for thin plates buckling on thick substrates in plane strain, independent of the expansion ϵ [3]:

$$k = \frac{1}{h_{\mathrm{BM}}} \left(\frac{E_{\mathrm{LP}}}{E_{\mathrm{BM}}} \frac{12(1 - \nu_{\mathrm{BM}}^2)(1 - \nu_{\mathrm{LP}})}{(1 + \nu_{\mathrm{LP}})(3 - 4\nu_{\mathrm{LP}})} \right)^{1/3}. \tag{8}$$

We now turn to the three-layer mucosa and assume that all layers are incompressible for simplicity ($\nu_{\mathrm{EP}} = \nu_{\mathrm{BM}} = \nu_{\mathrm{LP}} = 1/2$). Depending on how stiff and thick the added epithelial layer is, it will deform like another elastic medium analogous to the substrate (LP), or like another plate analogous to the BM. The plate-like mode entails a total energy density U_{p} that differs from that of the two-layered structure (Eq. 7) only in that it contains an analogous bending term for the EP:

$$U_{\mathrm{p}} = U_{\mathrm{LP}} + U_{\mathrm{BM}} + U_{\mathrm{EP}} = \frac{\epsilon}{3} \left(2 \frac{E_{\mathrm{LP}}}{k_{\mathrm{p}}} + \frac{1}{3} E_{\mathrm{BM}} h_{\mathrm{BM}}^3 k_{\mathrm{p}}^2 + \frac{1}{3} E_{\mathrm{EP}} h_{\mathrm{EP}}^3 k_{\mathrm{p}}^2 \right). \tag{9}$$

Minimizing Eq. 9 yields the ground state wavenumber

$$k_{\mathrm{p}} = \left(\frac{3 E_{\mathrm{LP}}}{E_{\mathrm{BM}} h_{\mathrm{BM}}^3 + E_{\mathrm{EP}} h_{\mathrm{EP}}^3} \right)^{1/3}, \tag{10}$$

which reflects the additivity of the two bending energies. Plate-like wrinkling requires the EP to be sufficiently stiff or thin, as otherwise it becomes energetically favorable for it to deform like an elastic medium similar to the

LP rather than bending along with the BM. We therefore consider a second (medium-like) mode of deformation for thick and compliant EP. For its energy density U_m, Eq. 7 needs to be extended by *two* terms: vertical deformation of the EP (as it acts like an elastic half-space analogous to the LP) and EP compression due to its volumetric expansion. Unlike in plate-like deformation, the EP cannot lengthen and therefore thickens vertically by the Poisson effect, which gives rise to the fourth energy term:

$$U_\mathrm{m} = U_\mathrm{LP} + U_\mathrm{BM} + U_\mathrm{EP} = \frac{\epsilon}{3}\left(2\frac{E_\mathrm{LP}}{k_\mathrm{m}} + \frac{1}{3}E_\mathrm{BM}h_\mathrm{BM}^3k_\mathrm{m}^2 + 2\frac{E_\mathrm{EP}}{k_\mathrm{m}} + 2E_\mathrm{EP}h_\mathrm{EP}\epsilon\right). \tag{11}$$

Minimizing Eq. 11 yields the ground state wavenumber

$$k_\mathrm{m} = \left(\frac{3(E_\mathrm{LP}+E_\mathrm{EP})}{E_\mathrm{BM}h_\mathrm{BM}^3}\right)^{1/3}, \tag{12}$$

which reflects the additive nature of the EP and LP stiffnesses in the medium-like deformation mode.

The plate-like and medium-like deformation modes contain mutually exclusive energy terms corresponding to different branches of an elastic instability. Based on the principle of energy minimization, the branch with lower elastic energy is favored and materializes as the mechanical ground state. The transition occurs when both energies are comparable. To identify the region in parameter space separating these two states, we therefore follow the standard approach of elastic stability analysis and equate the two elastic energy densities, $U_\mathrm{p} = U_\mathrm{m}$. This yields

$$\left(9\left(E_\mathrm{EP}+E_\mathrm{LP}\right)^2E_\mathrm{BM}h_\mathrm{BM}^3\right)^{1/3} + 2E_\mathrm{EP}h_\mathrm{EP}\epsilon = \left(9E_\mathrm{LP}^2\left(E_\mathrm{BM}h_\mathrm{BM}^3 + E_\mathrm{EP}h_\mathrm{EP}^3\right)\right)^{1/3}. \tag{13}$$

Introducing the stiffness and thickness ratios

$$r_\mathrm{EP} = \frac{E_\mathrm{EP}}{E_\mathrm{BM}}, \quad r_\mathrm{LP} = \frac{E_\mathrm{LP}}{E_\mathrm{BM}} \quad \text{and} \quad \widehat{h} = \frac{h_\mathrm{EP}}{h_\mathrm{BM}} \tag{14}$$

and rearranging the terms, the energy balance can be written entirely in terms of dimensionless quantities as

$$\left(r_\mathrm{EP}+r_\mathrm{LP}\right)^{2/3} + \frac{2}{3^{2/3}}r_\mathrm{EP}\widehat{h}\epsilon = r_\mathrm{LP}^{2/3}\left(1+r_\mathrm{EP}\widehat{h}^3\right)^{1/3}. \tag{15}$$

In Supplementary Fig. 3A, we plot the morphological boundary in the plane of stiffness ratios between the three layers for different amounts of volumetric expansion, ϵ, obtained by solving Eq. 15 numerically. For larger ϵ, the boundary shifts toward stiffer lamina propria, making the plate-like bending of the epithelium somewhat more favorable at large overgrowth of the upper two layers. Yet, both morphologies coexist also in the small-strain limit, in which the boundary is explicitly given by

$$r_\mathrm{LP} \to \frac{1+\sqrt{1+\widehat{h}^3r_\mathrm{EP}}}{\widehat{h}^3} \quad \text{for} \quad \epsilon \to 0. \tag{16}$$

In Supplementary Fig. 3B, the morphological regime boundary is plotted at different thickness ratios. Thicker epithelia (relative to the BM) allow for a larger region in the stiffness plane in which the medium-like deformation is favorable, suggesting that a transition from plate-like to medium-like deformation is possible also at fixed tissue stiffness, through a thinning of the BM, or a thickening of the EP.

In the mouse bladder, the BM thickness is likely in the order of 100 nm, whereas the EP thickness is in the order of 100 µm, such that $\widehat{h} \approx 1000$. This case is shown in Supplementary Fig. 3C, alongside the case of less tissue expansion ($\epsilon = 0.1$, Supplementary Fig. 3D), demonstrating that closer to the onset of differential tissue expansion and with a thinner BM, the transition from plate-like to medium-like deformation occurs at lower $E_\mathrm{LP}/E_\mathrm{EP}$ ratios.

Since the basement membrane is extremely thin in comparison to the other two tissue layers, the thin BM limit $\widehat{h} \to \infty$ is also of interest. Taking this limit in Eq. 15 yields a linear regime boundary

$$r_\mathrm{LP} \to \frac{2\sqrt{2\epsilon^3}}{3}r_\mathrm{EP} \quad \text{for} \quad \widehat{h} \to \infty. \tag{17}$$

In the considerations above, the optimal wavenumber for pure medium-like deformation, k_m, is always strictly greater than in pure plate-like deformation, k_p, as one can easily verify. In reality, however, the transition between the medium-like and plate-like buckling is not discontinuous, and as such, the regime boundary does not mark a sharp jump in behavior, but rather a smooth crossover. The patterning wavelength at the regime boundary thus cannot be found by imposing that $k_\mathrm{m} = k_\mathrm{p}$, but once again by equating the energy densities

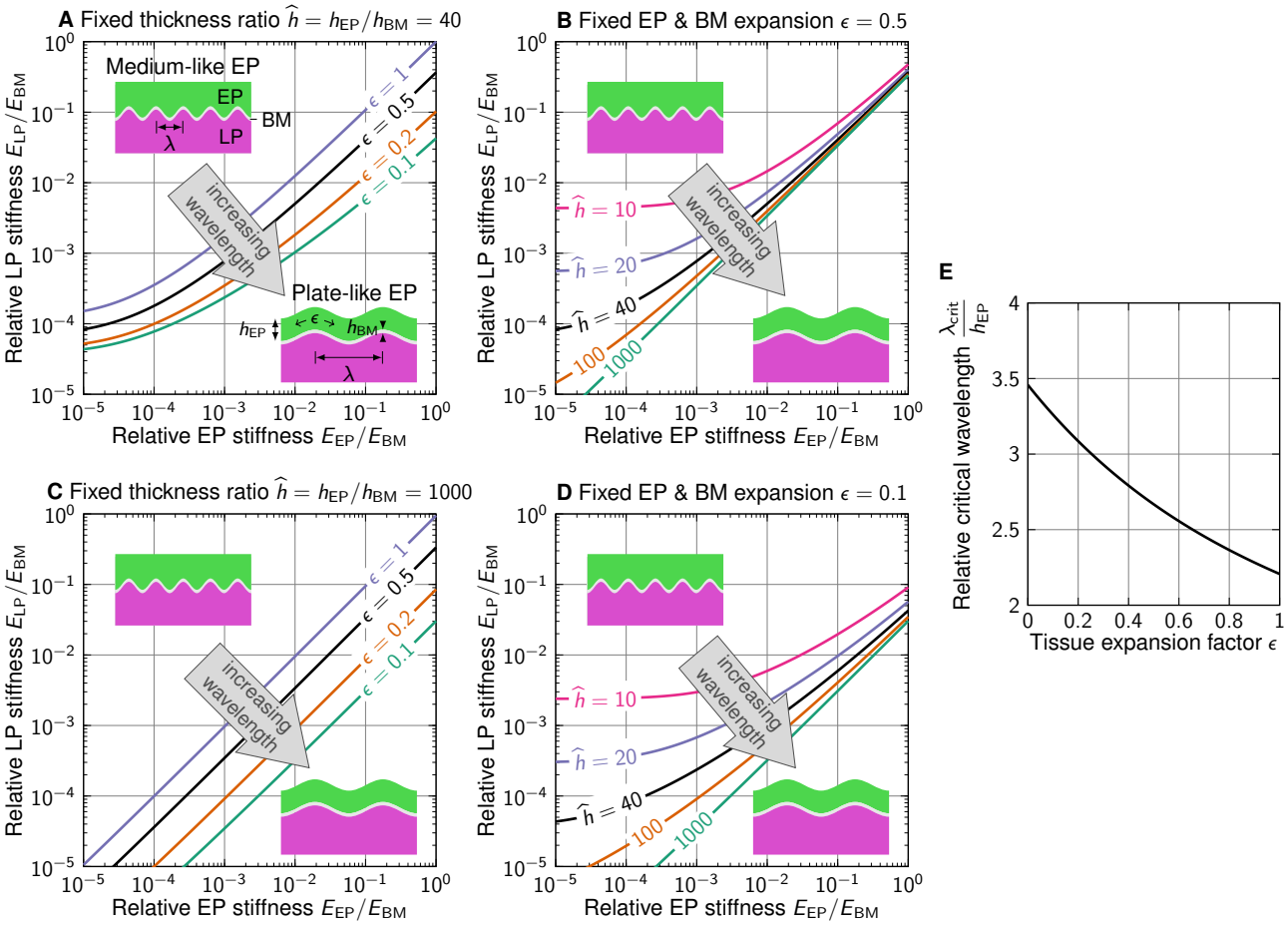

Supplementary Figure 3: Morphological transition between different epithelium folding regimes. **A** Theoretical boundaries between medium-like and plate-like deformations of the expanding epithelium at a fixed ratio of layer thicknesses $\widehat{h} = 40$, for different volumetric expansions. **B** Theoretical boundaries at a fixed volumetric expansion, for different thickness ratios. **C** Same as A but for thinner membranes, $\widehat{h} = 1000$. **D** Same as B but for lesser tissue expansion, $\epsilon = 0.1$. **E** Buckling wavelength at the regime boundary, Eq. 19.

$U_p = U_m$, now subject to the relaxed condition that the wavenumber is neither optimal for medium-like buckling ($k \neq k_m$) nor for plate-like buckling ($k \neq k_p$) when the crossover happens. This then leads to the depressed cubic equation

$$h_{EP}^3 k^3 - 6\epsilon h_{EP} k - 6 = 0 \tag{18}$$

from which one can find the critical wavelength at the regime boundary using Cardano's formula as long as $\epsilon < 3^{2/3}/2 \approx 1.04$:

$$\frac{\lambda_{crit}}{h_{EP}} = \frac{2\pi}{h_{EP} k} = \frac{2\pi}{\left(3 + \sqrt{9 - 8\epsilon^3}\right)^{1/3} + \left(3 - \sqrt{9 - 8\epsilon^3}\right)^{1/3}}. \tag{19}$$

This relationship is plotted in Supplementary Fig. 3E. Notably, the critical wavelength depends only on the thickness of the layer that changes its deformation mode (here, the epithelium), and the tissue growth difference, ϵ. At the onset of differential growth ($\epsilon \approx 0$), it evaluates to $\lambda_{crit} \approx 3.46 h_{EP}$, which is about 138 µm for an epithelium that is initially 40 µm thick. Later, when $\epsilon = 0.5$ as used in Fig. 5 and Supplementary Fig. 3, $\lambda_{crit} \approx 2.67 h_{EP} \approx 107$ µm. This is indeed the dominant wavelength that we observe in simulations in the vicinity of the boundary (Fig. 5D,E). For thicker epithelia, the critical wavelength at the regime boundary increases in proportion. At $h_{EP} = 100$ µm, for instance, $\lambda_{crit} \approx 267$ µm when $\epsilon = 0.5$.

As a final remark, we note that the layer stiffnesses and thicknesses occur only in the form of ratios (Eqs. 14, 19), not absolute numbers, which implies that this mechanical transition can be found across the scales. This may provide a common mechanical basis for the explanation of cancer formation in different multilayer tissues and across species. Medium-like deformation crumples the basement membrane at short wavelengths, potentially pushing it beyond the yield point at which plastic structural damage is dealt to the ECM. These short-wavelength folds in the basement membrane, together with irreversible damage and plastic stress localization, may provide a mechanical basis for the breach of the BM, and the onset of carcinomas in situ.

Supplementary References

[1] G. Papafotiou, V. Paraskevopoulou, E. Vasilaki, Z. Kanaki, N. Paschalidis, and A. Klinakis. KRT14 marks a subpopulation of bladder basal cells with pivotal role in regeneration and tumorigenesis. *Nat. Commun.*, 7:11914, 2016.

[2] M. A. Biot. Folding instability of a layered viscoelastic medium under compression. *Proc. R. Soc. Lond. A*, 242:444–454, 1957.

[3] J. Groenewold. Wrinkling of plates coupled with soft elastic media. *Physica A Stat. Mech. Appl.*, 298:32–45, 2001.